1.02 NASA Earth Observations

Angela M. Erb[a], Peter B. Boucher[a], Miguel O. Román[b], and Ian L. Paynter[a], [a] Leidos, Inc., Reston, VA, United States; and [b] NASA Goddard Space Flight Center, Greenbelt, MD, United States

© 2026 United States Government as represented by the Administrator of the National Aeronautics and Space Administration in all areas outside the United States of America. Published by Elsevier Inc.

This is an update of M.D. King, S. Platnick, 1.02—The Earth Observing System (EOS), Editor(s): Shunlin Liang, Comprehensive Remote Sensing, Elsevier, 2018, Pages 7—26, ISBN 9780128032213, https://doi.org/10.1016/B978-0-12-409548-9.10312-4.

1.02.1	**Introduction**	**9**
1.02.2	**Terra**	**12**
1.02.3	**Aqua**	**13**
1.02.4	**Aura**	**15**
1.02.5	**Suomi-NPP**	**15**
1.02.6	**Landsat 8 and Landsat 9**	**17**
1.02.7	**GPM**	**18**
1.02.8	**OCO-2**	**18**
1.02.9	**SMAP**	**19**
1.02.10	**DSCOVR**	**20**
1.02.11	**CYGNSS**	**21**
1.02.12	**GRACE-FO**	**21**
1.02.13	**ICESat-2**	**22**
1.02.14	**SWOT**	**23**
1.02.15	**TEMPO**	**24**
1.02.16	**TROPICS**	**24**
1.02.17	**ISS**	**25**
1.02.17.1	SAGE III ISS	25
1.02.17.2	TSIS-1	26
1.02.17.3	ECOSTRESS	27
1.02.17.4	GEDI	27
1.02.17.5	OCO-3	28
1.02.17.6	EMIT	28
1.02.18	**Summary and Conclusion**	**29**
Acknowledgements		**29**
References		**29**

Key Points

- NASA Earth observing satellites are essential to safeguard the continuity of critical Earth System Data Records and empower informed decision making.
- NASA Earth Science Division has grown its mission scope, science, and partnerships to support our understanding of and connections to our inhabited Earth.
- The NASA Earth Science Division has embraced new and innovative technologies and mechanisms to support the continued observation of the Earth's land, ocean and atmospheric systems.

Abstract

The NASA Earth Science Division (ESD) is part of the Science Mission Directorate and was established to advance understanding of Earth as an integrated system through space-based observations of Earth's atmosphere, land, oceans, and biosphere. In the mid-late 1980s, the Earth Observing System (EOS) was conceived and implemented as a series of large "flagship" missions and smaller focused satellites, often in partnership with instruments and spacecraft from other nations and agencies. The EOS launched is first mission in 1999 and subsequently 9 additional missions highlighted in the first edition of this chapter. In the years since, NASA ESD has expanded its mission scope, science, and partnerships to include national, international, commercial, and academic partners in the quest to better understand our Home Planet and deliver decision-ready science-quality data that strengthens resilience, supports economic security, and guides effective Earth system

management. These efforts safeguard the continuity of critical Earth System Data Records, which guide decisions related to long-term variability, extreme events, wildfire behavior, and global agricultural productivity among many other societal benefit areas.

1.02.1 Introduction

The development of the NASA Earth Observing System (EOS) can be traced back to 1980 and the establishment of the World Climate Research Programme (WCRP), an international effort to understand the physical basis of Earth's climate in response to droughts and floods, which revealed the linkage between societal vulnerability and climate variability. In subsequent years, the importance of having an integrated programmatic framework as a central paradigm of both national and international programs began to be recognized as crucial in the effort to understand earth and climate systems. Starting in 1985, a series of US National Research Council reports (National Research Council, 1985, 1986, 1988, 1990) called for an observing strategy that would focus on the highest priority measurements needed for each of the major disciplines of the Earth sciences. The reports stressed the need for simultaneous, calibrated, and continuous measurements that show how the Earth is changing, as well as the need to develop and validate global predictive models of the Earth's climate. This approach has since become foundational to delivering Earth science that serves the public good and informs national preparedness and environmental security goals. The Earth System Sciences Committee (ESSC), formed at NASA's (National Aeronautics and Space Administration) behest, wrote a seminal report that was released in two volumes (NASA Advisory Council, 1986; NASA Advisory Council, 1988). These reports, known collectively as the Bretherton reports in honor of the Committee Chairman Francis Bretherton, called for a program of sustained, long-term measurements of global environmental variables. The Committee stressed that the measurements must be coupled with focused studies on Earth system processes and the development of Earth system models. The program must also include an information system that would ensure open access to consistent, long-term observations of the Earth system.

In 1984 NASA formed several instrument panels to develop concepts for "facility instruments" that would provide comprehensive support to the scientific and applications communities, each with a supporting science team competitively selected via peer-review. An Announcement of Opportunity was released in 1988, and 3 types of proposals were solicited: (i) instrument investigations that would include the provision of instrumentation for flight on a polar platform, including non-Earth science payloads requiring polar orbits (PI instruments), (ii) research facility instrument team member and team leader investigations for facility instruments, and (iii) interdisciplinary science investigations to provide data analysis and modeling, which would prepare the community to use data acquired from the space platforms. The initial selections made in 1989 included support for 24 instrument investigations, 6 research facility instrument investigations, and 28 interdisciplinary investigations.

Although considerable changes were made over the years in the structure and orbital configuration of the various instruments and platforms, a total of 10 different missions were eventually flown, as shown in **Fig. 1**. These included three multi-instrument flagship platforms known as Terra (launched in 1999), Aqua (launched in 2002), and Aura (launched in 2004). The Terra mission emphasis was primarily on land processes, Aqua on the hydrological cycle, and Aura on atmospheric chemistry. In addition to these flagship missions, the EOS missions included Landsat 7 (which measured land cover classification and change), QuikSCAT (wind speed and direction over the oceans), Jason-1 (ocean surface topography and sea level), ACRIMSAT (total solar irradiance (TSI)), SAGE III (stratospheric aerosol and ozone levels), ICESat (ice, cloud, and land elevation), and SORCE (total and spectral solar irradiance).

These first 10 missions set the stage for an expansive fleet of subsequent Earth observing missions that have continued to record and provide invaluable data and insight on Earth systems. Of the 10 missions initially highlighted in the first edition of this chapter, only the three flagship platforms (Terra, Aqua, and Aura) remain operational, each representing over 20 years of near continuous Earth observations. The current fleet, as shown in **Fig. 2** (c. 2025), consists of 17 active, free-flying satellites and 6 instruments mounted to the observational arms of the International Space Station (ISS).

When developing new missions, NASA considers continuity with previous data records, technological advances, and the evolving needs of the user communities, balancing future technological needs with the preservation of the historical value of heritage sensor data through continuity with past missions. New missions represent an opportunity to measure Earth's systems at higher spatial, temporal, spectral, angular, and radiometric resolutions, producing data with a broader range of applications and improving the accuracy of predictive models. All the science data products produced by these missions are available without charge throughout the world. As such, NASA Earth Science Data Records are highly valued for their many contributions to modeling and monitoring applications, supporting evaluations of air quality, fires, land cover change, and the state of the oceans. As part of NASA's Earth Action strategy, EOS missions now play a central role in connecting long-term satellite data with real-time environmental challenges, from local hazard response to global-scale decision frameworks. These missions have also operated in support of recording Essential Climate Variables (ECVs), which are key physical, chemical, and biological indicators that have been recognized by the Global Climate Observing System (GCOS) as critical for understanding and characterizing Earth's climate. The 55 ECVs recognized by GCOS and the NASA Earth observing sensors that support their observations are shown in **Table 1**.



Fig. 1 Schematic illustration of the 10 different spacecraft that constitute NASA's Earth Observing System program, all of which were launched between 1999 and 2004.

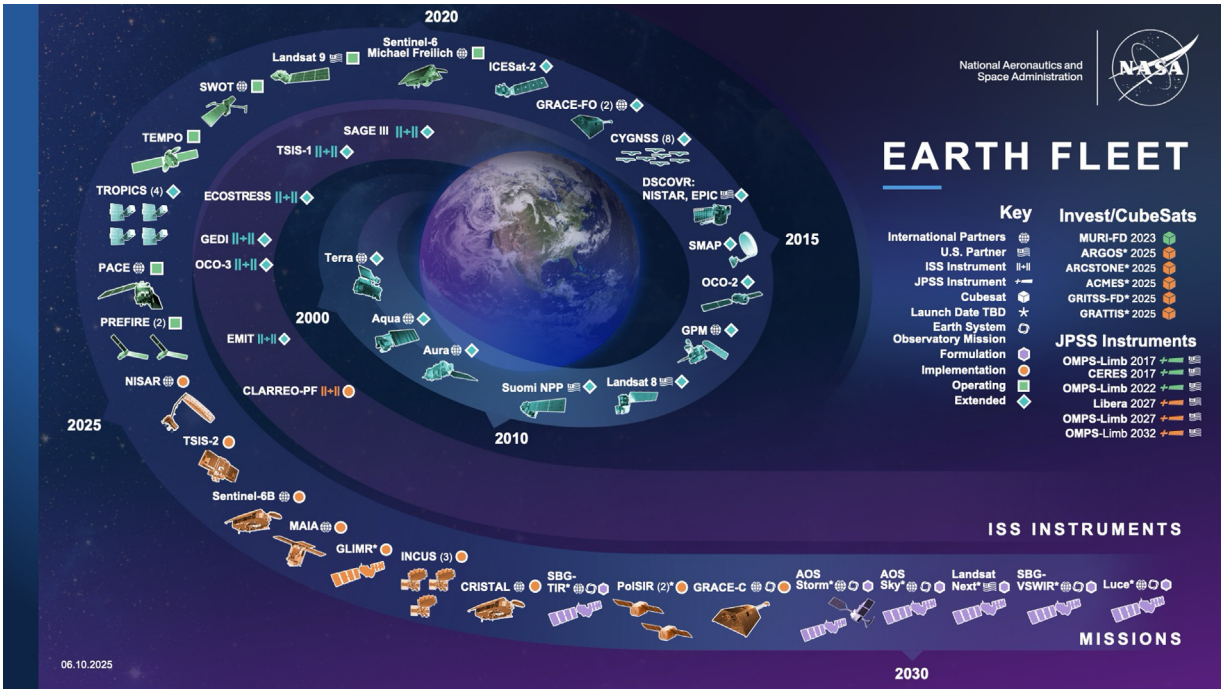


Fig. 2 Schematic illustration of the fleet of the NASA's Earth Science program, all of which were launched between 1999 and 2024. Produced by NASA Headquarters.

Over the last few decades, the historical record of Earth's systems collected by EOS sensors has proven essential for scientific research, industrial applications, and the general advancement of society. For example, these missions and measurements have fueled innovation in extreme weather prediction (e.g., see GPM for extreme precipitation monitoring and CYGNSS for hurricane formation), greenhouse gas monitoring (e.g., see OCO-2, OCO-3, and EMIT's quantifications of atmospheric carbon dioxide and methane), and measuring the shape, structure, and mass of the planet (e.g., see ICESat-2's measurements of ice loss, GEDI's

Table 1 Key physical variables needed to advance understanding of the entire Earth system and the interactions among the components.

	Domain	*Essential climate variable*	*Active sensors*
Atmosphere	Surface	Precipitation	GMI, DPR, AMSR-E, CrIS
		Pressure	KaRIN
		Surface radiation budget	MODIS, VIIRS, OLI/OLI-2, NISTAR, EPIC
		Surface temperature	VIIRS, TIRS/TIRS-2, PHyTIR
		Surface water vapor	OMPS, TIRS/TIRS-2, AMR-S
		Wind speed and direction	SWOT, SMAP, AMSR-E, DDMI, DPR, GMI
		Upper-air temperature	MODIS, AIRS, MLS, HIRDLS, TES, TROPICS
	Upper air (troposphere)	Earth radiation budget	CERES, MODIS, VIIRS, OLI, OLI-2, SAGE III, AIRS, ATLAS, MISR, AIRS, EMIT
		Lightning	VIIRS, TEMPO
		Water vapor	SAGE III ISS
		Wind speed and direction	CYGNSS
	Atmospheric composition	Clouds	MODIS, VIIRS, ASTER, MISR, AIRS, AMSR-E, CERES, SAGE III ISS, TROPICS
		Aerosols	MODIS, VIIRS, TEMPO, SAGE III ISS, TEMPO, HIRDLS
		Carbon dioxide, methane & other greenhouse gases	MOPITT, AIRS, MLS, HIRDLS, TES, OMI, OCO-2/OCO-3, EMIT, TROPICS
		Ozone	TEMPO, MLS, HIRDLS, TES, OMI, OMPS, TEMPO
		Precursors for aerosols & ozone	
Land	Hydrosphere	Groundwater	GRACE-FO
		Lakes	MODIS, VIIRS, OLI/OLI-2, ICESAT-2, Poseidon 3C, KaRIN
		River discharge	Poseidon 3C, KaRIN
		Terrestrial water storage	GRACE-FO, ICESAT-2
		Evaporation from land	PHyTIR
		Soil moisture	TIRS, AMSR-E, SMAP radar and radiometer
	Cryosphere	Glaciers	ASTER, GRACE-FO, OLI/OLI-2, ICESAT-2
		Ice sheets & ice shelves	ASTER. GRACE-FO, ICESAT-2
		Permafrost	SMAP radiometer
		Snow	VIIRS, MODIS, ASTER, DPR, GMI, GRACE-FO, AMSR-E, OLI/OLI-2
	Biosphere	Above-ground biomass	GEDI, ATLAS
		Albedo	MODIS, VIIRS, VIIRS, OLI/OLI-2
		Fire	ASTER, MODIS, VIIRS, OLI/OLI-2
		Fraction of absorbed photosynthetically active radiation	MODIS, VIIRS, OLI/OLI-2, EPIC, OCO-2/OCO-3
		Land cover	ASTER, MODIS, VIIRS, MISR, OLI/OLI-2
		Land surface temperature	ASTER, MODIS, VIIRS, AIRS, TIRS/TIRS-2, PHyTIR
		Leaf area index	MODIS, VIIRS, OLI/OLI-2, EPIC, GEDI
	Anthroposphere	Anthropogenic greenhouse gas fluxes	MOPITT, AIRS, MLS, HIRDLS, TES, OMI, OCO-2/OCO-3, EMIT, TEMPO
		Anthropogenic water use	ACC, LRI, SMAP, KaRIN, Poisidon-3C
Ocean	Physical	Ocean surface heat flux	
		Sea ice	MODIS, VIIRS, ASTER, AMSR-E, OLI/OLI-2, ICESAT-2, Poseidon 3C, KaRIN
		Sea level	ICESAT-2, Poseidon 3C, KaRIN
		Sea state	
		Sea surface currents	AMSR-E, DDMI, Poseidon 3C, KaRIN
		Sea surface salinity	
		Sea surface stress	
		Sea surface temperature	MODIS, VIIRS, AMSR-E
		Subsurface currents	
		Subsurface salinity	
		Subsurface temperature	
	Biogeochemical	Inorganic carbon	
		Nitrous oxide	
		Nutrients	
		Ocean color	MODIS, VIIRS, OLI/OLI-2
		Oxygen	
		Transient tracers	
	Biological/Ecosystems	Marine habitats	OLI/OLI-2
		Plankton	MODIS, VIIRS

global forest structure assessments, and GRACE-FO's measurements of variation in the Earth's mass). Collectively, data from these sensors have built up our current understanding of our planet in flux, empowering communities, government agencies, and industries with the tools needed to respond effectively to environmental change. These efforts are laying an invaluable foundation of measurements that will be a boon to future generations of scientists, industry professionals, and societal leaders who strive to understand and respond to our changing world.

In this article we will describe a selection of the currently active NASA Earth observing missions, highlighting their groundbreaking sensor design and contributions to the scientific community. Several sensors are also discussed in more detail in later chapters of this volume.

1.02.2 Terra

Terra was the first EOS multi-instrument flagship spacecraft. It launched in December 1999 and flew at an altitude of 705 km in a sun-synchronous polar orbit with a descending 10:30 a.m. (morning) equator crossing time. Terra was designed with a six-year lifespan, but in December 2025, Terra will mark 25 years of near continuous Earth observation. After two and a half decades, however, Terra is nearing its end-of-life. In 2020, Terra completed its final inclination maneuver to maintain its stable orbit. Since then, the satellite has been in a free drift phase with the equatorial crossing time occurring progressively earlier in the morning. Onboard instruments have been continuing to collect high-quality science data, as the validation, calibration, and science teams have been monitoring and managing the impact of changing acquisition parameters on downstream data products.

Initially known as EOS AM-1 because of its morning observations of the Earth system, Terra provides global data on the state of the atmosphere, land, ocean, and cryosphere, as well as their interactions with solar radiation. Terra's observation time was chosen to capture observations of the land surface (hence the name "Terra") during the morning, when there were typically fewer clouds than in the afternoon. That said, subsequent observations from Terra have shown that while cloud cover is indeed lower over the land during the morning, it is greater over the oceans at this time of day (King et al., 2013).

Terra was built with five state-of-the-art instruments: ASTER (provided by the Japanese Ministry of Economy, Trade and Industry); MOPITT (provided by the Canadian Space Agency); and CERES, MISR, and MODIS (all provided by NASA). These instruments, with characteristics summarized in **Table 2**, record data for many different applications, including (i) digital elevation models of the land's topography at high spatial resolution (up to 7 m absolute horizontal and vertical accuracy) (Abrams et al., 2015); (ii) thermal observations of volcanoes and monitoring the extent and change of global land ice (glaciers) (Abrams et al., 2015); (iii) monitoring the radiation budget of the Earth (both longwave and shortwave, and net radiation) and assessing the impact of natural (e.g., El Niño) and human-caused changes on the radiation budget (Loeb and Wielicki, 2015); (iv) aerosol and cloud optical and radiative properties (King et al., 2013; Levy et al., 2013); (v) the percent of the Earth's surface that is covered by clouds (King et al., 2013); (vi) carbon monoxide associated with man's activities and fires (Deeter et al., 2014); (vi) large-scale changes in the biosphere, both ocean and land, and global productivity (Verma et al., 2014); (vii) land and ocean surface temperature (Kilpatrick et al., 2015) (viii) the vertical distribution of temperature and water vapor in the atmosphere (King et al., 2003); (ix) the areal extent of snow and ice (Hall et al., 2010); (x) vegetation health and the seasonal change in vegetation cover (Friedl et al., 2010); (xi) angular reflectance distribution of various surfaces (Liu et al., 2009); (xii) fires and burn scars (Giglio et al., 2013); and (xii) chlorophyll fluorescence (Behrenfeld et al., 2009) which can help assess the energy efficiency of photosynthesis of ocean biota.

The MODIS instrument is one of the most highly used instruments, in large part because of its multidisciplinary capability to study the oceans, land, and atmosphere, and to aid in various natural hazard assessments, such as (i) fires, (ii) severe storms, (iii) floods, (iv) dust, smoke, and haze, and (v) crops and droughts. A comprehensive description of its various calibrators and their operational utility and performance can be found in Xiong et al. (2016). During on-orbit operations, the aperture door cover is opened so that the double-sided scan mirror can scan across track of the orbit to obtain reflected and emitted radiation in a swath 2330 km across the orbital path, thereby providing nearly complete coverage of the globe each day, with only minor gaps in the equatorial region between 30° North and South.

With the Terra mission, and all subsequent missions of EOS, the selected science team members charged with producing Earth system science data products from their instruments were required to develop a prelaunch algorithm theoretical basis document (ATBD) that would describe in some detail the granules and metadata to be included, all internal and external data product flows to be utilized, a physical and mathematical description of the algorithm, variance or uncertainty estimates, and practical considerations, such as calibration and validation, exception handling, quality control, and diagnostics. The ATBD was then subjected to both written and oral reviews from a worldwide panel of expert scientists charged to assess the validity and maturity of the approach to algorithms being developed. This review aimed to assist the algorithm developers in validating their approaches, as well as to gain community acceptance of the science team's approach well in advance of detailed algorithm coding. ATBDs also serve to document instrument-specific algorithms for the community of users who make use of NASA's data products in studies of the Earth system and applications that extend beyond the life-span of the instrument. In the years since launch, the ATBD has evolved to include an extensive suite of data products that are produced by the satellite's science teams and distributed by NASA. These products encompass a wide range of surface processes and have been used in modelling, monitoring, and forecasting studies, with data from Terra serving as a community standard for land, atmosphere, and ocean observations.

Table 2 Key characteristics of the Terra instruments.

Instrument	*Measurement technique*	*Characteristics*
ASTER[a]	VNIR subsystem	3 spectral bands
	Pushbroom radiometer	Spatial resolution: 15 m
		Swath width: 60 km
		Backward telescope for stereo
	SWIR subsystem	6 spectral bands
	Whiskbroom radiometer	Spatial resolution: 30 m
		Swath width: 60 km
	TIR subsystem	5 spectral bands
	Whiskbroom radiometer	Spatial resolution: 90 m
		Swath width: 60 km
CERES (2)	Thermistor bolometers	3 spectral bands
	3 separate telescopes per instrument	Shortwave window (SW, 0.3–5 μm)
	2 separate instruments	Infrared window (WN, 8–12 μm)
	Cross-track scanner	Total (TOT, 0.3–200 μm)
	Rotating azimuth scanner	Spatial resolution: 20 km
		Swath width: Limb to limb
MISR	Nine CCD-based pushbroom radiometers	4 spectral bands (0.44–0.87 μm)
	Fixed at nine viewing angles	9 viewing directions (70.5° fore—70.5° aft)
		Spatial resolution: 275 m, 440 m, or 1.1 km (selectable in flight)
		Swath width: 360 km
MODIS	Whiskbroom spectroradiometer	36 spectral bands
		20 bands (0.41–2.1 μm)
		16 bands (3.75–14.2 μm)
		Spatial resolution
		250 m resolution (2 bands)
		500 m resolution (5 bands)
		1000 m (29 bands)
		Swath width: 2330 km
MOPITT[b]	Gas correlation radiometer	3 spectral bands using both pressure and length modulated gas cells
		Spatial resolution: 22 km
		Swath width: 640 km

1.02.3 Aqua

Aqua is the second, multi-instrument EOS flagship spacecraft, and for most of its mission, it has been orbiting at an altitude of 705 km in a sun-synchronous polar orbit with an ascending 1:35 p.m. (afternoon) equator crossing time (Parkinson, 2003). It launched in early May 2002 and has been acquiring near-continuous observations for over 20 years (Parkinson, 2022). In January 2022, Aqua left its designated orbit and began its free drift phase, beginning a slow descent with no further positioning movements planned. The onboard instruments have continued to collect data, and the science and calibration teams have worked to maintain data continuity with shifting acquisition geometries and conditions.

Initially known as EOS PM-1 because of its afternoon observations of the Earth system, it can be viewed as a companion to Terra, providing global data on the state of the atmosphere, land, ocean, and cryosphere, with a special emphasis on water in all its forms and on the hydrological cycle (hence the name Aqua). While not originally envisioned to fly as part of a satellite constellation, Aqua became the first platform in the NASA-led international Afternoon constellation (A-Train) (L'Ecuyer and Jiang, 2010), allowing for synergistic measurements from a variety of passive and active sensors.

Aqua carries six separate Earth observing instruments: AIRS, AMSU, CERES (two copies), and MODIS (all provided by NASA), HSB (provided by INPE, Brazil's National Institute for Space Research), and AMSR-E (provided by JAXA). The Aqua instruments characteristics are summarized in **Table 3**. The CERES and MODIS instruments are identical to those on Terra while the AIRS, AMSU, and HSB suite of sounding instruments, meant to have their measurements processed jointly, are primarily focused on deriving atmospheric profiles of temperature and water vapor. Additionally, they provide retrievals of numerous other variables, including key trace gases in the atmosphere, such as ozone and carbon dioxide (Aumann et al., 2003; Chahine et al., 2006, 2008), and multiple cloud properties (Kahn et al., 2014). Because HSB failed in 2003, the AIRS/AMSU/HSB science team revised their retrieval algorithms to continue data collection and science data processing despite the loss in this instrument capability. To

Table 3 Key characteristics of the Aqua instruments.

Instrument	*Measurement technique*	*Characteristics*
AIRS	Grating spectrometer	2378 spectral channels 2378 channels within three infrared bands (3.74–4.61, 6.20–8.22, and 8.8–15.4 μm) Spatial resolution: 13.5 km Swath width: 1650 km
	Visible/near-infrared imager	4 spectral bands Shortwave (0.40–0.94 μm) Spatial resolution: 2.3 km Swath width: 1650 km
AMSU	Microwave sounder	15 spectral bands 23–90 GHz (0.3–1.3 cm) Spatial resolution: 40.5 km Swath width: 1650 km
HSB[a]	Microwave sounder	4 spectral bands 150–190 GHz (0.16–0.2 cm) Spatial resolution: 13.5 km Swath width: 1650 km
AMSR-E[b]	Dual polarization passive microwave radiometer Conically scanning	12 spectral bands (6 frequencies each with 2 polarizations) 6.9–89 GHz (0.33–4.3 cm) Spatial resolution From 6 km × 4 km (89 GHz) to 74 km × 43 km (6.9 GHz) Swath width: 1445 km
CERES (2)	Thermistor bolometers 3 separate telescopes per instrument 2 separate instruments Cross-track scanner Rotating azimuth scanner	3 spectral bands Shortwave window (SW, 0.3–5 μm) Infrared window (WN, 8–12 μm) Total (TOT, 0.3–200 μm) Spatial resolution: 20 km Swath width: Limb to limb
MODIS	Whiskbroom spectroradiometer	36 spectral bands 20 bands (0.41–2.1 μm) 16 bands (3.75–14.2 μm) Spatial resolution 250 m resolution (2 bands) 500 m resolution (5 bands) 1000 m (29 bands) Swath width: 2330 km

guard against future ASMU failures the science team also devised AIRS-only retrievals. AMSR-E is a passive microwave radiometer that does not require sunlight, and several of its channels are unaffected by clouds, allowing probing of the surface irrespective of day/night or cloud-cover conditions. Although it suffered a major malfunction in October 2011, by that time it had provided a long time series of sea surface temperature (Gentemann et al., 2010), including cold wakes following the passage of hurricanes, sea ice seasonal and interannual variation in the Arctic and Antarctic (Comiso et al., 2008; Comiso and Hall, 2014; Parkinson and Comiso, 2008), soil moisture, and global precipitation. In addition, its applications included retrievals of integrated water vapor, cloud liquid water, and snow water content (Parkinson, 2013). To provide data record continuity, JAXA launched an advanced version of AMSR-E into the A-Train in May 2012 (AMSR2 on GCOM-W1).

The AIRS instrument is the prime instrument for atmospheric sounding in the original EOS fleet. This instrument consists of a diffraction grating that disperses the radiation from the scene onto 17 linear arrays of Mercury Cadmium Telluride (HgCdTe) detectors on the focal plane and is cooled to 60 K by a Stirling/pulse tube cryocooler. The IR spectrometer is cooled to 155 K by a passive radiative cooler. A full description of the AIRS instrument can be found in Aumann et al. (2003). During on-orbit operations, the aperture door cover is opened so that the scan mirror can scan across track of the orbit to obtain emitted radiation in a swath 1650 km across the orbital path. The AIRS instrument also includes four visible/near-infrared channels between 0.40 and 0.94 μm with a 2.3 km field of view.

Table 4 Key characteristics of the Aura instruments.

Instrument	*Measurement technique*	*Characteristics*
HIRDLS[a]	Limb infrared filter radiometer	21 spectral bands 6.2–17.76 μm Vertical resolution: 1.2 km Swath width: 10 km
MLS	Microwave limb sounder GHz radiometer (118–640 GHz) THz radiometer (2.25 THz) Spectrometer module	5 spectral bands 118 GHz–2.52 THz Vertical resolution: 1.5 km Swath width: 3 km
OMI[b]	Hyperspectral pushbroom radiometer UV-1 spectrometer (270–310 nm) UV-2 spectrometer (310–365 nm) Visible spectrometer (365–504 nm)	780 spectral bands (270–504 nm) Spatial resolution: 13 km × 24 km Swath width: 2600 km
TES	Infrared-imaging fourier-transform spectrometer	Spectral coverage: 3.3–15.4 μm Spatial resolution: 0.53 km × 5.3 km Swath: 5.3 km × 8.5 km

1.02.4 Aura

Aura is the third, multi-instrument EOS flagship spacecraft, and was launched to fly at 705 km in an ascending 1:45 p.m. (afternoon) equator crossing time (Schoeberl et al., 2006). It entered its free drift phase 2023 and is now slowly drifting, but like Terra and Aqua, is still collecting quality science data. Initially known as EOS CHEM-1 because of its focus on atmospheric chemistry, it has an identical spacecraft bus (common spacecraft) to Aqua and houses a suite of atmospheric instruments. It was renamed Aura (Latin for breeze) as a complement to the names Terra and Aqua, its predecessor flagship missions. At launch, Aura became the second member of the A-Train constellation.

Aura launched in 2004 and has four separate Earth observing instruments: MLS and TES (both provided by NASA), OMI (provided by the Netherlands Space Office (NSO) in collaboration with the Finnish Meteorological Institute (FMI)), and HIRDLS (provided as a partnership between NASA and the UK Rutherford Appleton Laboratory). MLS and OMI continue to operate and collect science-quality data as of this writing, while HIRDLS and TES ended data collection in 2008 and 2018, respectively. These instruments, with characteristics summarized in **Table 4**, were designed to contribute to a wide range of science applications. All the instruments measure atmospheric composition, with OMI primarily providing column concentrations of O3 (McPeters et al., 2015), NO2 (Duncan et al., 2016), SO2 and aerosol index (Torres et al., 2007). MLS, a microwave limb sounder, provides profiles of stratospheric water vapor and ozone as well as atmospheric radicals important to O3, such as ClO, and also N2O, HCl, and HNO3 (Waters et al., 2006). HIRDLS measured vertical profiles of O3, HNO3, CFC-11, and CFC-12 (Gille et al., 2005), while TES focused on tropospheric profiles of O3, CO, H2O, CO2, CH4, and NH3, to name a few (Beer, 2006).

OMI is the prime instrument for monitoring total ozone content and tropospheric SO2 and NO2 on EOS. This instrument is a pushbroom imaging spectrometer with three channels in visible and ultraviolet spectral range (350–500 nm, 270–314 nm and 306–380 nm). The OMI sensor features a wide-field telescope and depolarizer which remove the polarization from the backscattered radiation. The incoming spectral signal is split by dichroic beam splitters and onto a diffraction grating that images the radiation onto two charge-coupled device (CCD) arrays in the visible and ultraviolet regions. The UV channel consists of two subchannels (UV-1 and UV-2). The image on the CCD array is 580 pixels cross track (2600 km) × 780 spectral wavelengths for the UV and visible channels. The full performance range is 270–500 nm. A full description of the OMI can be found in Levelt et al. (2006).

1.02.5 Suomi-NPP

The Suomi National Polar-Orbiting Partnership (Suomi-NPP/S-NPP) was launched in October of 2011 as part of the National Polar-Orbiting Environmental Satellite System (NPOESS) Preparatory Project (NPP) which was renamed to Suomi National Polar-orbiting Partnership after launch. The satellite was named to honor Verner E. Suomi, a meteorologist considered the father of satellite meteorology and inventor of the spin scan radiometer. The mission was developed as a collaboration between NASA, NOAA, and the Department of Defense to bridge the gap between the Aqua and Terra missions and the Joint Polar Satellite System missions (see Chapter 4). Like Aqua, Suomi-NPP has a sun-synchronous afternoon orbit with a local overpass time at the equator of 1:30pm. It orbits at 824 km and circles the Earth roughly 14 times per day with a repeat period of 16 days.

Suomi-NPP is a multi-instrument mission and houses 5 instruments: CERES (FM5), ATMS, CrIS, OMPS and VIIRS. Instrument specifications are shown in **Table 5**. The CERES sensor is the fifth (FM5) of six active CERES instruments with two each on Terra and Aqua and the sixth launched in 2014 on NOAA-20. CERES-FM5 has a slightly larger footprint than the first four instruments at 24 km but shares their spectral configuration of a shortwave, infrared window channel and total radiation channel. The final CERES

Table 5 Key characteristics of the Suomi-NPP instruments.

Instrument	*Measurement technique*	*Characteristics*
ATMS	Microwave sounder	22 spectral bands 23.8–18.31 Ghz Spatial resolution: ~45 km Swath width: 1650 km
CERES		3 spectral bands
	Thermistor bolometers	Shortwave window (SW, 0.3–5 μm)
	3 separate telescopes	Infrared window (WN, 8–12 μm)
	Cross-track scanner	Total (TOT, 0.3–200 μm)
	Rotating azimuth scanner	Spatial resolution: 24 km Swath width: Limb to limb
VIIRS	Pushbroom spectroradiometer	22 spectral bands 15 bands (0.4–2.28 μm) 7 bands (3.5–12.5 μm) Spatial resolution 375 m resolution (5 bands) 750 m (17 bands) Swath width: 3060 km
CrIS	Fourier transform michelson interferometer	1305 spectral channels 1305 channels within three infrared bands (3.92–4.64, 5.71–8.26, and 9.14–15.4 μm) Spatial resolution: 14 km Swath width: 2200 km
OMPS	3 UV hyperspectral imaging spectrometers	Spectral coverage: 0.29–1.0 μm
	Nadir mapper (0.30–0.38 μm)	Bandwidth: 1 nm
	Nadir profile (0.25–0.31 μm)	Spatial resolution: 50 km, 250 km, < 2 km
	Limb sounding (0.29–1.0 μm)	Swath: 2800 km, 250 km, 250 km

instrument (FM6) was launched on NOAA-20 and replaced the WN channel with a longwave channel (5–35 μm), more information on this mission can be found in Chapter 4. The ATMS, CrIS and OMPS sensors build vertical profiles of atmospheric temperature, composition and moisture for use in short- and medium-term weather forecasting, storm tracking and climate prediction models (Tobin et al., 2013; Yang et al., 2013; Han et al., 2013; Pan et al., 2017).

The launch of Suomi-NPP marked the beginning of the end of the MODIS era as the sensor was functionally replaced with the Visible Infrared Imaging Radiometer Suite (VIIRS). Compared to MODIS, the VIIRS sensor has a greater swath width (eliminating coverage gaps), fewer bands (22) and lower gridded spatial resolution (375/750 m). The 22 VIIRS bands include 5 imaging (I-bands) with a spatial resolution of 375 m at nadir, 16 moderate resolutions (M-bands) at 750 m at nadir, and 1 day-night-band (DNB) which is optimized to observe dim/weak illumination sources, also at 750 m resolution. VIIRS scans a 3000 km × 12 km swath using a rotating telescope assembly (RTA) which houses an afocal three mirror anastigmat telescope and fold mirror and has a rotation period of 1.78 seconds. The incoming rays are directed through the half-angle mirror (HAM) which rotates at half the speed of the RTA and de-rotates the beam into the aft-optics assembly (AOA). The aft-optics assembly is distributed across four focal plane assemblies, two VISNIR detectors, one SMIR detector and one LWIR detector. The visible and near-IR light is then reflected to a separate VISNIR/DNB (Day Night Band) focal plane filter assembly which is immediately above the detectors.

In contrast with MODIS, seven of the VIIRS bands have dual gain capabilities which are controlled by the focal plane electronics and independently calibrated. This provides the sensor with a larger dynamic range and allows more accurate observations where reflectance is either very low (e.g., surface water) or very high (e.g., snow, ice, clouds). The day-night-band is further specialized with multiple gain settings and filtering techniques to optimize the acquisition of low-light imagery during different lunar phases. The DNB sensor operates with a central wavelength of 700 nm and a 200 nm bandwidth. The wide dynamic range required for nighttime acquisitions is captured by a set of 4 detector arrays with 3 different radiometric gain capabilities (low gain stage (LGS), middle gain stage (MGS), and 2 high gain stage (HGS)). The 2 high gain stages (HGA and HGB) are duplicated to identify and correct for the impact of stray light during acquisition. The gain difference between the HGS and MGS is about 2 orders of magnitude, while the overall HGS radiometric gain difference from the LGS is about 5 orders of magnitude. The signals from all 4 arrays are digitized and the most appropriate value is selected using logical operations (JPSS ATBD, 2011). The VIIRS DNB has allowed for a more comprehensive measurement of nocturnal light in the visible to near infrared range and marks significant improvement in resolution and calibration from the previous Defense Meteorological Satellite Program (DMSP). VIIRS DNB products have been used to detect impacts of severe weather events (Román et al., 2019; Wang et al., 2018), urban expansion (Román et al. 2018), sub-pixel scale

fires (Polivka et al., 2016), anthropogenic activities (e.g. Fishing vessels, gas flares; Asanuma et al., 2016; Elvidge et al., 2015) and provide information on nighttime atmospheric properties (Minnis et al., 2016; Walther et al., 2013; Johnson et al., 2013; McHardy et al., 2015; Wang et al., 2016).

The expanded capabilities of the VIIRS sensors have provided the opportunity for new and advancing applications. Also, the VIIRS Science Team has successfully prioritized the development of NASA land and ocean products to provide continuity with the heavily used MODIS product suite (Román et al., 2024). Continuity of the ESDRs will continue as Suomi-NPP was followed by NOAA-20 and NOAA-21, launched in 2017 and 2022 respectively. More information in these satellites and the NOAA remote sensing program can be found in Chapter 4.

1.02.6 Landsat 8 and Landsat 9

Landsat 8 and Landsat 9 are the latest in a long line of Landsat satellites dating back to 1972. Landsat 8, originally called the Landsat Data Continuity Mission (LDCM), launched in 2013 (Irons et al. 2012; Loveland and Irons 2016), and Landsat 9 launched in 2021 (Masek, 2020). Both orbit in sun-synchronous near polar orbits at an altitude of 705 km. The instrument orbits are offset by 8 days, each with a 16-day repeat cycle and an equatorial crossing time of 10:00 a.m. ± 15 minutes. Combined, Landsat 8 and 9 collect ~1500 scenes per day, equivalent to the Eurasia landmass. The NASA/USGS Landsat Program provides the longest continuous space-based record beginning with the launch of Landsat 1 in 1972 (originally the Earth Resource Technology Satellite) and continuing forward with the planned launch of Landsat Next, expected no earlier than 2031. Each new satellite comes with advances in the technical and imaging capabilities of the instrument, ensuring that Landsat remains a critical tool for the global community while maintaining continuity with its uniquely long data record.

Landsat 8 and 9 each host two sensors: an Operational Land Imager (OLI/OLI-2 respectively) and a Thermal Infrared Sensor (TIRS/TIRS-2 respectively). The OLI sensors differ from the predecessor Landsat 7 ETM+ with the addition of a "Coastal/Aerosol Band" (band 1) useful for capturing shallow water and tracking atmospheric particles and a "Cirrus Band" (band 9) used in detecting high-altitude, thin clouds and improving cloud detection algorithms. Landsat 8 and 9 sensors also have increased radiometric resolution (12 bit and 14 bit respectively) and spectrally narrower bands, which enables greater precision in the spectral signatures, better calibration, and lower signal to noise ratios. The TIRS sensors record two thermal infrared bands designed to measure land surface temperature through a split-window technique that assists in distinguishing between surface temperature and atmospheric temperature. The OLI and TIRS instrument specifications are shown in **Table 6**.

Uses of the Landsat 8 and 9 measurements, as well as the historical record obtained from the earlier Enhanced Thematic Mapper (ETM+) on Landsat 7 and Thematic Mapper (TM) measurements on Landsat 4 and 5, have allowed diverse studies of land, ocean and ice systems. Some of Landsat's science applications are highlighted by Wulder et al. (2019), including: (i) cryosphere science including snow, ice and glacier dynamics, (ii) aquatic science, water quality indicators and dynamic surface water mapping, (iii) vegetation phenology in agriculture and forest systems, (iv) surface albedo and land surface temperature modeling (v) water use, evapotranspiration and crop yields, and (vi) forest monitoring. A more comprehensive history of the 50 years of the Landsat Science Program and its contributions can be found in a book entitled "Landsat's Enduring Legacy" (Goward et al., 2017), in Chapter 3 of this volume and Wulder et al. (2022).

Table 6 Key characteristics of the Landsat 8 and Landsat 9 instruments.

Instrument	*Measurement technique*	*Characteristics*
OLI/OLI-2		9 spectral bands 8 bands (0.43–1.38 μm)
	Pushbroom radiometer OLI: 12 bit resolution OLI-2: 14 bit resolution	1 band (0.503–0.676 μm) Spatial resolution 30 m resolution (6 bands) 15 m resolution (1 band) Swath width: 185 km
TIRS/TIRS-2	Pushbroom radiometer	2 thermal bands 2 bands (10.6–12.51 μm) Spatial resolution 100 m (2 bands) Swath width: 185 km

Table 7 Key characteristics of the GPM Core instrument.

Instrument	*Measurement technique*	*Characteristics*
GMI	Dual-polarization passive microwave radiometer	13 microwave bands (10.65–183.3 GHz) Spatial resolution: 11 km Swath width: 885 km
DPR	Dual frequency radar	2 radar bands Ku-band (13.6 GHz) Ka-band (35.5 GHz) Spatial resolution: 5 km (nadir) Swath width: 245 km

1.02.7 GPM

The Global Precipitation Measurement (GPM) mission is a satellite constellation that tracks rain and snow globally. The mission was initiated by NASA and JAXA as a successor to TRMM (1999–2015) in collaboration with several international space agencies including CNES, ISRO, NOAA and EUMETSAT. The mission is composed of a core satellite that serves as a reference standard to support other operational and research satellites. The GPM Core Observatory was launched in February 2014 and carries a Ku/Ka-band Dual-frequency Precipitation Radar (DPR) and a multi-channel GPM Microwave Imager (GMI). It has a circular, non-sun-synchronous orbit at 408 km ($\pm$ 11 km) at in inclination 65°, providing data globally at 3-h increments.

The DPR sensor consists of a Ka-band precipitation radar (KaPR) operating at 35.5 GHz and a Ku-band precipitation radar (KuPR) operating at 13.6 GHz. Originally the swath widths varied with data collected over a swath of 125 and 245 km for the Ka and Ku band radars respectively, but as of May 2018 both swaths were reset to 245 km. The radar instruments are aligned to capture the same 5 km footprint simultaneously using a variable pulse repetition frequency (VPRF) technique which enables a higher sampling rate. The two radar soundings provide a three-dimensional reconstruction of precipitation, including information on particle drop size distributions over moderate precipitation intensities and estimation of rainfall rates with 0.2 mm/h sensitivity. The DPR and GMI instrument specifications are shown in **Table 7**.

The GMI instrument is a multi-channel, polarization-sensitive, conical-scanning microwave radiometer covering a swath of 885 km. It serves as the critical records standard for the satellites that make up the GPM constellation. The GMI uses a set of 13 frequencies ranging from 10 GHz to 183 GHz to distinguish precipitation type and intensity. It detects the polarization differences at each channel and uses that as an indicator of the optical thickness and water content in precipitation systems. From this information it is possible to characterize precipitation type and intensity, cloud structure, and in-cloud precipitation. It is an off-nadir instrument with the cone sweep set to 48.5°. The GMI receives data with a 1.2 m antenna and spins at 32 rotations per minute. Its swath is centered on the observatory's ground track vector and the 245 km swath of the DPR instrument.

Data from the GPM Core are used to generate the Integrated Multi-Satellite Retrievals for GPM (IMERG) data products which incorporate various available IR, microwave (MW), and gauge observations. This multi-instrument and multi-agency approach allows for precipitation estimates at relatively high spatial ($0.1\,^{\circ} \times 0.1\,^{\circ}$) and temporal resolution (30 min) (Huffman et al., 2015). NASA's GPM mission and IMERG data products serve a broad swath of applications and science directives that influence ecological and human health and safety. GPM data have been used in weather forecasting models to improve precipitation estimates during monsoon events (Zhang et al., 2019) and hurricanes (Pu et al., 2019). The data has also been used to validate and improve precipitation dynamics in climate models (Tapiador et al., 2017; Adirosi et al., 2016; Colle et al., 2017) and are valuable for agricultural planning, water resource management (Kirschbaum,et al., 2017), and disaster response, helping to optimize water usage and improve resilience to natural hazards (Wu et al. 2014; Schumann et al., 2016).

1.02.8 OCO-2

The Orbiting Carbon Observatory-2 (OCO-2) launched in 2014 as a follow-up to the OCO mission, which was lost in a launch failure in 2009. OCO-2 is a passive radiometer designed to study carbon and is a member of the A-train satellite constellation with Aqua and Aura. The OCO-2 orbit is a near-polar sun synchronous orbit at 705 km altitude. It collects data using a pushbroom scanning configuration with a swath width of 10 km and footprint of 1.29 km cross-track and 2.25 km along-track at nadir ($\pm$ 1 km based on view angle; Crisp et al., 2008). OCO-2 houses three co-boresighted, long-slit, imaging grating spectrometers which passively measure radiances and use the unique signatures of gas absorption to model the mole fraction of carbon dioxide (XCO_2) in the atmospheric column and Solar-Induced chlorophyll Fluorescence (SIF), the latter being an important proxy for monitoring plant productivity. The instruments record (i) an Oxygen A-band (O_2A/ABO_2) with a spectral wavelength of

Table 8 Key characteristics of the OCO-2 instrument.

Instrument	*Measurement technique*	*Characteristics*
OCO-2	3 long-slit imaging grating spectrometers	3 NIR bands (0.76–0.77, 1.59–1.62, 2.04–2.08 μm) Spectral resolution: (0.04, 0.08, 0.10 nm) Spatial resolution: 1.29 × 2.25 km Swath width: 10 km

758–772 nm and spectral resolution of 0.04, (ii) a weak carbon dioxide band (weak CO_2/WCO_2) with a spectral wavelength of 1594–1619 nm and a spectral resolution 0.08 nm, and (iii) a strong carbon dioxide band (strong CO_2/$SCO_{2)}$ with a spectral wavelength of 2042–2082 nm and spectral resolution of 0.10 nm. The spectrometers are built into a shared optical bench assembly and use a single 200 mm focal length, F/1.8 Cassegrain telescope. Incoming light is focused and recollimated before entering the relay optics assembly where the light is redirected by dichroic beam splitters to the targeted channels (Crisp et al., 2008). The instrument specifications are shown in **Table 8**.

The OCO-2 instrument can operate in 3 viewing modes acquiring nadir, glint, and target acquisitions. Nadir mode is the primary acquisition configuration in which observations are taken with the instrument pointed straight down to collect data along the ground track. In glint mode, the sensor is positioned such that the viewing angle is equal to the angle of reflection of the incident sunlight in order to capture the bright spot that occurs where solar radiation is specularly reflected from the surface. In 2015, the OCO-2 retrieval strategy was optimized to collect glint and nadir retrievals in alternating orbits and to always collect glint observations over ocean-only orbits (Crisp et al., 2017). In target mode, the instrument maintains its view of a target surface location and collects measurements as it orbits overhead. In nadir or glint mode, OCO-2 observes eight adjacent footprints that span the swath (<10 km) of the instrument field of view and collects 24 soundings per second (Crisp et al., 2008). Target mode is often used for validation exercises in locations where ground measured XCO_2 measurements are recorded.

The primary science objective of the OCO-2 mission is to retrieve column-averaged dry-air mole fractions of carbon dioxide. These measurements have enabled further understanding of the annual growth rate of X_{CO2} (Pandey et al., 2024) and large-scale carbon dynamics (Crowell et al., 2019; Peiro et al., 2022; Byrne et al., 2023). OCO-2 data has been used to capture the global and regional impacts of extreme anomalies, like droughts, floods and wildfires (Parazoo et al., 2024; Feldman et al., 2023; Yin et al., 2020; Byrne et al., 2021; Jiang et al., 2021), El Niño and La Niña (Chatterjee et al., 2017; Liu et al., 2024a, b), and anthropogenic sources of atmospheric carbon (Nassar et al., 2017; Wu et al., 2020; Hu and Shi, 2021; Wilmot et al., 2024). In addition, OCO-2 also provides information about the Solar-Induced chlorophyll Fluorescence (SIF), a proxy for the uptake of CO_2 by the biosphere, or gross primary production (GPP). SIF is measured by looking at shifts in Fraunhofer lines, dark bands in the solar spectrum formed by light absorbing elements in the solar atmosphere or interstellar medium. The OCO-2 O_2A band, at 757-775 nm, is within the SIF emission spectrum (660-850 nm) and contains a few relatively deep solar Fraunhofer lines. The in-filling of these bands with reflected radiation from the earth's surface enables the detection and measurement of SIF emissions and can be used to estimate GPP (Sun et al., 2022; Doughty et al., 2021; Zhang et al., 2023a, b, c; Feldman et al., 2024). The stable, long-term, and high-quality data record from OCO-2 makes it truly unique among all sensors measuring atmospheric CO_2, including missions operated by international space agency partners. This has been made possible by the continued efforts of the calibration, retrieval, and validation teams to not just meet but exceed the original baseline mission science requirements. The latest data version from OCO-2 surpasses the precision requirement (0.3% or 1.2 ppm on regional scales) yielding single-sounding accuracy near 0.5 ppm and precision <1 ppm (Das et al., 2025).

In 2019, OCO-3 was launched to the International Space Station (ISS) in a complementary mission utilizing spare parts from the original OCO-2 build, more details on this sensor can be found in **OCO-3** section of this chapter.

1.02.9 SMAP

The Soil Moisture Active Passive (SMAP) mission was launched in January 2015 to measure soil moisture and freeze/thaw state using an active L-band radar and passive L-band radiometer. The L-band radar (VV, HH, and HV polarizations) emits radio waves centered at 1.26 Ghz and measures soil moisture in the top five inches soil layer by measuring the backscatter reflected to the receiver. The passive L-band radiometer (V, H, and third and fourth Stokes parameter polarizations) measures radio waves centered at 1.41 Ghz naturally emitted by the earth. The instruments use a large scanning 6-m antenna feedhorn and reflector which spins at 14.6 revolutions per minute. The observatory orbits at 685 km, in a near polar, sun-synchronous 6 a.m./6 p.m., 8-day exact repeat frozen orbit. The sensors image a 1000 km-wide swath providing global coverage every 2 to 3 days.

The L-band radar failed in July 2015 after collecting three months of data, however, the coincident radar and radiometer measurements provided insight on the value of the combined active and passive sensor approach and benefits of higher resolution soil moisture measurements. The passive radiometer has continued to operate and produce global freeze/thaw maps at 36 km resolution every 2–3 days. The primary SMAP science mission ended in 2018, but the instrument has continued to collect data in an

Table 9 Key characteristics of the SMAP instrument.

Instruments	*Measurement technique*	*Characteristics*
SMAP	Active L-band radar	1.26 Ghz Swath width: 1000 km
	Passive L-band radiometer	1.41 Ghz Spatial resolution: 36 km Swath width: 1000 km

operational capacity. Full instrument specifications are shown in **Table 9**. SMAP data products include daily composites of soil moisture and freeze/thaw states and model-derived value-added data products that support key SMAP applications. SMAP products have been applied to a wide range of scientific and management applications including agricultural drought monitoring (Mladenova et al., 2019), rapid flood detection (Rahman et al., 2019), carbon budgets (Endsley et al., 2020), wildfire (Goffin et al., 2024; Alizadeh et al., 2024), global evapotranspiration (Purdy et al., 2018; Walker et al., 2019; Kim et al., 2023) and forest system health (Colliander et al., 2020). Additionally, SMAP radiometer data has contributed to ocean science applications through sea surface salinity and wind speed measurements and the tracking of cyclones, typhoons and temperature anomalies.

1.02.10 DSCOVR

The Deep Space Climate Observatory (DSCOVR) is a joint mission between NASA, NOAA, and the US Air Force (USAF) originally developed in 1998. The mission was put on hold in 2001, but it was revived and refurbished in 2008 and launched in February 2015. DSCOVR orbits around the first Sun-Earth Lagrange point (L1), roughly 1.5 million kilometers inside the Earth's orbit of the sun in a tilted (Lissajous) orbit. The L1 is a stable position where the gravitational forces of the Earth and sun cancel each other out, allowing the continuous observation of the sunlit half of the Earth with minimal positioning assistance. The spacecraft carries three instruments, EPIC (Earth Polychromatic Imaging Camera), NISTAR (National Institute of Standards and Technology Advanced Radiometer), and the PlasMag (Plasma Magnetometer) Instrument suite. The instruments specifications are shown in **Table 10**. DSCOVR continuously monitors the solar wind to give real time forecasting of geomagnetic disturbances due to solar wind transients.

EPIC is a ten-channel UV/VIS/NIR radiometer which is used to record atmospheric, land and ocean properties including ozone and aerosol levels, cloud and vegetation properties, and ultraviolet radiation estimates (Marshak et al., 2018). The instrument's 10 channels have central wavelengths between 317–779 nm and varying bandwidths of 0.8–3.0 μm. Due to its Lissajous orbit around the L1 point, the angular size of the Earth changes from 0.45–0.53° within the 6-month orbital period. EPIC records imagery with a 30-cm aperture Cassegrain telescope. The incoming light is focused by a primary and secondary mirror array through a Field Lens Group (FLG) which uses a 2048 × 2048 pixel CCD. The imagery is averaged onboard and downlinked as 1024 × 1024 pixel images for most wavelengths with a rough spatial resolution of 20 km at the equator. The targeted wavelengths are isolated using a double filter wheel with 12 spaces housing 10 filters and 2 open holes. The filters are positioned using stepper motors in a pre-determined sequence that can be manipulated by ground operators. EPIC produces a complete picture of the sun-lit earth every 65–110 minutes and measures numerous physical and chemical properties. These data products, distributed by NASA, include ozone and aerosol concentrations and dynamics (Xu et al., 2017), sulfur dioxide from volcanic emissions, UV Aerosols Index (UVAI), cloud mask, height and thickness, atmospheric correction parameters (Lyapustin et al., 2021), vegetation indices (Hao et al., 2020; Yang et al., 2017), ocean surface PAR, sun glint parameters (Varnai et al., 2021), and aerosol heights.

Table 10 Key characteristics of the DSCOVR instrument.

Instrument	*Measurement technique*	*Characteristics*
EPIC	Spectroradiometer	10 spectral bands: 0.317–0.779 μm Spectral resolution: 0.8–3.0 μm Spatial resolution: 10 km Swath width: 3060 km
NISAR	3 active cavity radiometers	3 spectral bands: 0.2–100 μm, 0.2–4.0 μm, 0.7–4.0 μm Spatial resolution: 2.5 km Swath width: 3060 km
PlasMag	Faraday cup solar wind positive ion detector Fluxgate vector magnetometer Top-hat electron electrostatic analyzer	Solar wind proton density, velocity, and temperature Heliospheric vector magnetic fields Solar wind electron characteristics

Also onboard the DSCOVR platform is NISTAR, which has the same footprint as EPIC, but uses three active cavity (or electron substitution) radiometers to measure the radiance output of the sunlit Earth at varying wavelengths. The instrument was designed and developed by NIST (National Institute of Standards and Technology) and has a 1° field of view to capture the entire sunlit earth in a single measurement. The radiometers cover three different spectral ranges: (i) 0.2−100 μm for measurement of the total radiant power emerging from the Earth, (ii) 0.2−4.0 μm for measurement of the total reflected solar radiance, and (iii) 0.7−4.0 μm for measurement of the fraction of solar radiance reflected in the NIR, SWIR, and part of the MWIR spectrums (Su et al., 2020). Uniquely, the radiance is measured by converting the received signal to heat and determining its magnitude by the fluctuations in the heating power required to maintain the instrument's cavity temperature.

The PlasMag Instrument suite is a space weather monitor that includes a fluxgate vector magnetometer, a Faraday Cup and a top-hat electron electrostatic analyzer. The Faraday cup measures the accumulation of positively charged particles to determine solar wind velocity, density, and temperature. The solar wind plasma and magnetic fields influence Earth geomagnetic system creating geomagnetic storms causing power, communication, and satellite system disruptions (Loto'aniu et al., 2022).

1.02.11 CYGNSS

The Cyclone Global Navigation Satellite System (CYGNSS) is a constellation of eight microsatellites launched in December of 2016 as a collaboration between NASA and the University of Michigan and was part of the Earth System Science Pathfinder program and Earth Ventures Program. CYGNSS makes continuous global measurements of ocean surface winds and tropical cyclones to determine how they form and evolve. The eight CYGNSS satellites, instrument specifications shown in **Table 11**, orbit in a common orbit plane at 520 km altitude in a non-sun-synchronous orbit with an inclination of 35°, covering between 38 N and 38S. Each satellite houses a Delay Doppler Mapping Instrument (DDMI) which uses an L-band receiver at 1.6 GHz to measure both the direct signals from GPS systems and the time delay and frequency shifts of GPS signals reflected off the ocean surface. The direct signals are used to track the location of the CYGNSS observatory, while the reflected signals correspond to ocean surface roughness, from which wind speed is estimated using a Geophysical Model Function (GMF). CYGNSS is used to study meteorological processes and improve numerical weather forecasts with a focus on tropical cyclone inner core processes. The CYGNSS data enables scientists to monitor the rapidly changing air-sea interaction processes near the inner core of storms, which influence hurricane formation, development, and intensity. In addition to ocean systems, CYGNSS is used to study inland water bodies dynamics (Carreno-Luengo et al., 2024) and land surface processes including soil moisture, flood inundation (Zeiger et al., 2022), and above ground biomass (Santi et al., 2020). A comprehensive overview of the CYGNSS Science Team efforts can be found in Carreno-Luengo et al. (2021).

1.02.12 GRACE-FO

The Gravity Recovery and Climate Experiment Follow-On (GRACE-FO) mission is a collaboration between NASA and the German Research Centre for Geosciences (GFZ). GRACE-FO is a successor to the original GRACE mission (2002−2017) and launched in May of 2018. It is composed of two nearly identical satellites in the same nearly circular polar orbit, launched at 490 km altitude (Landerer et al., 2020). The satellites are separated in orbit by 170−270 km and each carries a microwave ranging system, the Microwave Instrument (MWI). The MWI operates a 24 Ghz (K-band) and 32 Ghz (Ka-band) microwave transmitter and receiver to communicate with its satellite "twin" to continuously measure their separation distance to 1 μm precision (Kornfeld et al., 2019). The fluctuations in this distance caused by Earth's varying gravitational forces are recorded. Each satellite is georeferenced with satellite GPS receivers to track its location, and an accelerometer at its center of mass which measures accelerations by outside forces (e.g. atmospheric drag or thruster firings).

GRACE-FO also carries an experimental Laser Ranging Interferometer (LRI) which performs the same function as the MWI but uses first-in-space laser interferometry instead of microwaves. The LRI was developed jointly between the JPL and the Max Planck Institute for Gravitational Physics Albert Einstein Institute (AEI) and Space Tech (STI) in Germany and emits approximately 25 mW of light at 1064 nm. The LRI has maintained continuous operations since launch with comparable accuracy to the MWI but a higher

Table 11 Key characteristics of the CYGNSS instruments.

Instrument	*Measurement technique*	*Characteristics*
DDMI	L-band receiver	1.6 Ghz Spatial resolution: 0.5 km (specular) 25 km (diffuse) Swath width: 25 km

Table 12 Key characteristics of the GRACE-FO instruments.

Instrument	*Measurement technique*	*Characteristics*
ACC	Accelerometer	
MWI	2 frequency microwave interferometer	K-band (24 Ghz) Ka-band (32 GHz)
LRI	Laser ranging interferometer	Spatial resolution: 300-500 km

sensitivity to anomalies in the static gravity fields at higher spatial resolutions (Ghobadi-Far et al., 2020). The specifications for both instruments are shown in **Table 12**.

As of 2025, GRACE and GRACE-FO together have provided a 23-year data record of Earth's changing gravity field and mass change observations. These data precisely track changes in terrestrial water storage (TWS) at local, regional, and global scales, providing insights and understanding of the cyclical, seasonal, annual, and long-term causes and processes influencing water resources, including groundwater storage and flood potential. Additionally, the measurements are used to track seasonal and long-term changes in the mass changes of polar ice sheets and mountain glaciers, and to provide improved predictions of anticipated future changes. GRACE(−FO) estimates have quantified the ice mass loss from the Antarctic Ice Sheet, Greenland Ice Sheet, glaciers and ice caps cumulatively as upwards of 600 Gt/year between 2002 and 2019 (Velicogna et al., 2020; Ciracì et al., 2020). These data also measure the subsequent changes in ocean mass and its contribution to sea level change resulting from this freshwater exchange (Chang and Sun, 2022; Sun et al., 2022). Beyond water near Earth's surface, the measurements track land mass changes resulting from large earthquake events, as well as provide insight on the movement of the Earth's mantle, particularly related to still-ongoing glacial isostatic adjustment (Tanaka, 2023; Kadrolli and Kalnoor, 2024). GRACE-mission data are an essential element in the development of novel terrestrial reference frames that provide an enduring foundation for monitoring changes in the geoid and sea levels, as well as allowing for precision orbit determination for satellites (Haines et al., 2024). A more comprehensive review of GRACE operations, applications and technical specification can be found in Chen et al. (2022).

1.02.13 ICESat-2

ICESat-2 is the successor to ICESat (2003−2009) and was launched in September 2018. It houses the Advanced Topographic Laser Altimeter System (ATLAS), a LiDAR (Light Detection And Ranging) system that uses a 532 nm laser and emits 10,000 pulses per second (**Table 13**). The sensor measures the height profile of ground objects to provide information on surface topography and structure. Each ATLAS pulse is split into 6 beams arranged into 3 pairs. This allows the instrument greater ground coverage and the ability to measure the slopes of surfaces. The configuration and pulse rate enables ICESat-2 to record measurements every 2.3 feet along the satellite's ground path. The reflected laser pulses are captured by a 2.6 foot diameter beryllium telescope specifically aligned by a novel Laser Reference System (LRS). ICESat-2 orbits at an altitude of 500 km in a 92° inclination that provides coverage between 88 N and 88S. It repeats its ground track every 91 days. The high inclination angle was designed to ensure coverage over the West Antarctic ice sheet in the southern hemisphere and the Arctic sea-ice extent in the northern hemisphere using the intersections of both ascending and descending passes (Schutz et al., 2005). ICESat-2 was designed with four primary science objectives in mind: (i) to measure ice sheet mass changes and the contribution to sea level rise, (ii) to quantify the regional evolution of ice sheet change, (iii) to study sea ice thickness, and (iv) to measure vegetation height in forest and vegetated ecosystems globally. The applications of ICESat-2 data have expanded beyond these initial science objectives to include enhanced characterization of clouds and aerosols (Herzfeld et al., 2021; Markus et al., 2017; Palm et al., 2021), land topography (Neuenschwander et al., 2020), shallow and near coastal bathymetry (Parrish et al., 2019; Babbel et al., 2021), and ocean and inland water body elevation (Ryan et al., 2020; Buzzanga et al., 2021).

Table 13 Key characteristics of the ICESat-2 instrument.

Instrument	*Measurement technique*	*Characteristics*
ATLAS	Laser altimeter	Light detection and ranging (lidar) at 0.532 μm Pulse repetition frequency: 10 kHz Laser surface spot size: 11 m

1.02.14 SWOT

The Surface Water and Ocean Topography (SWOT) mission, developed by NASA and CNES in collaboration with the Canadian and United Kingdom Space Agencies, aims to provide the first global survey of Earth's surface water, including both the oceans and inland waters. Launched in December 2022, the satellite orbits at an altitude of 890 km, covering latitudes between 78°N and 78°S. SWOT's orbit is non-sun-synchronous, designed to minimize alignment with tidal cycles while optimizing the observation of the major ocean basins and inland water bodies such as rivers, lakes, and wetlands. The satellite's primary instrument is Ka-band Radar Interferometers (KaRIn), which consists of two synthetic aperture radar antennas operating in tandem, mounted on either side of a 10-m mast. Each sensor records radar pulses reflected from 2 50 km wide swaths, offset by 10 km from the nadir. The KaRIn height measurements are complemented by four additional sensors located on the nadir core of the satellite: (i) a Jason-class nadir altimeter (Poseidon-3C), which measures water surface height along the center of the 20 km gap between the KaRIn footprints; (ii) a three-channel microwave radiometer (AMR-S) that measures atmospheric water content; (iii) a laser reflector assembly (LRA); and (iv) a Doppler Orbitography and Radiopositioning Integrated by Satellite (DORIS) system for precise orbital tracking (**Table 14**). After its launch in 2022, SWOT underwent a 90-day commissioning phase, followed by a "fast-sampling" phase in which it repeated the same orbital path with a 1-day repeat cycle and 14 orbits per cycle at an altitude of 857 km. This phase was designed to validate and calibrate the novel KaRIn sensors and track rapidly changing phenomena. In July 2023, SWOT transitioned to its operational orbit at 891 km, providing global coverage with a 21-day repeat cycle and an average revisit time of 11 days.

To measure the sub-mesoscale properties of oceans and inland water bodies, water elevation must be captured with centimeter-scale accuracy. The KaRIn instruments achieve this using synthetic aperture radar (SAR) interferometry and wide-swath altimetry. Wide-swath altimetry employs radar pulses at a near-nadir incidence angle to measure surface water height across the pulse footprint, offering extensive spatial coverage and eliminating coverage gaps. KaRIn's dual swath interferometer alternates between sending radar pulses in horizontal (H) or vertical (V) linear polarization, with the right and left swaths corresponding to each polarization. To accomplish this, the swath interferometer uses an offset dual-feedhorn, allowing each reflectarray antenna to generate two separate beams (in H or V polarization) that are emitted ± 2.65 degrees off boresight. The pulse returns are recorded by receivers on both KaRIn sensors, and the different angular configurations of the returns enable a more accurate and precise two-dimensional mapping of surface water topography. The radar has a pulse length of 6.4 μs with a central frequency of 35.75 GHz and a 200 MHz bandwidth. The spatial resolution ranges from approximately 70 m at the near edge of the swath to 10 m at the far end, with a 2.63-m resolution in the in-track direction.

This sensor design, coupled with an optimized acquisition strategy, enables more frequent global coverage of both oceanic and continental water surfaces, including lakes, reservoirs, wetlands larger than 250×250 m^2, and rivers as narrow as 100 m or potentially smaller. With high-precision measurements, KaRIn can assess ocean topography, from which the velocity of ocean currents driven by surface slopes can be computed. It can also provide valuable insights into short-term climate events, such as the El Niño and La Niña phases of the El Niño Southern Oscillation (ENSO), as well as longer-term phenomena like the Pacific Decadal Oscillation (PDO). Additionally, the sensor is capable of tracking terrestrial water inundation (Smith et al., 2023; Laipelt et al., 2025), monitoring water movement through river systems (Larnier et al., 2020) and assessing flood risk and impacts in coastal regions (Buis, 2024). The innovative technology and enhanced measurement resolution open a wide range of other applications, including the mapping and modelling of ocean bathymetry, sea ice freeboard, tsunami detection, tidal system analysis, and wave generation (Fu et al., 2024; Srinivasan and Tsontos, 2023; Yu et al., 2021).

Table 14 Key characteristics of the SWOT instrument.

Instrument	*Measurement technique*	*Characteristics*
KaRIn	2 Ka-band radar interferometers	Ka-band (35.75 GHz) 8.4 mm wavelength
Poseidon-3C nadir altimeter	Dual-frequency radar altimeter	2 spectral bands 13.6 GHz (2.2 cm) 5.3 GHz (5.7 cm)
AMR-S	Microwave radiometer	3 spectral bands 18.7, 23.8, 34 GHz
LRA	Laser retroflector array	9 suprasil quartz retroreflectors
	Passive reflector	Receives laser signals from ground sources
DORIS	Precision orbit-determination system	Receiver measures Doppler shift at 2 frequencies transmitted

1.02.15 TEMPO

The Tropospheric Emissions: Monitoring Pollution (TEMPO) instrument is a collaboration between NASA and the Smithsonian Astrophysical Observatory that was the first selection from the NASA Earth Venture Instrument Program (EVI-1) within the Earth System Science Pathfinder Program (ESSP). It launched aboard Intelsat-40e (IS-40e), a commercial communications satellite positioned at 91° W, in April of 2023, and its first images were received in August of 2023. The TEMPO sensor is a high-resolution grating spectrometer sensitive to visible and ultraviolet wavelengths that is used primarily to monitor atmospheric pollution. TEMPO is in a geostationary (GEO) orbit at approximately 35,400 km in altitude, which enables it to scan east to west across North America once an hour during daylight hours.

The TEMPO field of regard (FOR) is at centered 33.5° N, 89.2° W and it captures data over much of North America between 65°W and 120°W and roughly between 17° and 60° N. The TEMPO sensor scans the FOR in approximately 1181 steps, producing imagery with a spatial resolution of 2 km north-south and 4.7 km east-west at center. The instrument assembly sits on the Earth-facing side of IS-40e and includes: (i) the Calibration Mechanism Assembly (CMA) which controls the instrument aperture, (ii) the Scan Mechanism Assembly (SMA) which steps the instrument field of view across the field of regard from east to west and adjusts for spacecraft movement, (iii) the Opto-Mechanical Subsystems, consisting of the telescope and spectrometer assembly (see **Table 15**), and (iv) the Focal Plane Array (FPA) and Focal Plane Electronics (FPE).

One of the primary challenges in the design and implementation of TEMPO was ensuring accurate image navigation and registration (INR). To achieve accurate registration, the SMA operates a closed-loop control using real-time altitude data from IS-40e. This information is supplemented by ground processing protocols which link known tie-points in TEMPO imagery to the more accurately registered GOES imagery acquired with a latency of less than 5 min (Zoogman et al., 2017). The high spectral, temporal and spatial resolution coupled with the INR technologies enable the sensor to measure atmospheric concentrations of ozone (O3), nitrogen dioxide (NO2), sulfur dioxide (SO2), formaldehyde (H2CO), glyoxal (C2H2O2), bromine monoxide (BrO), IO (iodine monoxide), water vapor, HONO (nitrous acid), aerosols, cloud parameters, ultraviolet radiation, ocean color and vegetation foliage properties. The sensor can capture diurnal cycles of emissions and track how pollutants move across the country. TEMPO measurements can improve both short- and long-term air quality forecasts that have direct implications for human health (Zoogman et al., 2014, 2017). In addition to the daily sweeps across North America, TEMPO can enter a non-standard operations mode to focus on specific events like wildfires, dust storms, volcanic eruptions, and acute contamination events at higher temporal resolution (e.g., 10 min). At night, TEMPO can observe nighttime lights such city lights, nightglow, aurorae, gas flaring, and lightning (Carr et al., 2024)

1.02.16 TROPICS

The Time-Resolved Observations of Precipitation structure and storm Intensity with a Constellation of Smallsats (TROPICS) mission was developed under the NASA Earth Venture Instrument Program (EVI-3) in collaboration with the Massachusetts Institute of Technology (MIT) Lincoln Laboratory to monitor tropical regions and track how storm systems form and evolve. The TROPICS mission is built around a constellation of small, identical 3-unit (3U) CubeSats, comprised of a 2U Blue Canyon Technologies spacecraft bus and a 1U payload housing a compact cross-track scanning passive millimeter-wave spectrometer measuring in the W/F/G bands. The primary instrument payload, named the TROPICS Millimeter-wave Sounder (TMS), measures microwave radiances at 12 channels near the atmospheric absorption features of oxygen and water vapor (**Table 16**). The TMS features an offset

Table 15 Key characteristics of the TEMPO instrument.

Instrument	*Measurement technique*	*Characteristics*
TEMPO	2 spectrometers Ultraviolet spectrometer (293-494 nm) Visible spectrometer (537-741 nm)	Spectral sampling: 0.2 nm Spectral resolution: 0.6 nm Spatial resolution: 2 km North/South, 4.75 km East/West

Table 16 Key characteristics of the TROPICS instrument.

Instrument	*Measurement technique*	*Characteristics*
TROPICS	12-Channel (W/F/G) passive microwave radiometer	W Band 92 GHz F Band 117—119 GHz G band 183 & 204 GHz

parabolic reflector with separate feedhorns for the W/F and G-band receivers. The instrument scans by spinning the entire 1U payload in a cross-track pattern over the surface.

The TROPICS constellation was launched to an initial orbit of 550 km at an inclination angle of about 30°, resulting in a median revisit time of 1 hour. Without onboard propulsion, the CubeSats gradually descend over about two years, leading to longer revisit times before decommissioning and reentry. The initial high temporal resolution and microwave technology enables the instruments to capture rapidly evolving storm environments, including temperature and moisture content of the atmosphere as well as precipitation rates at meso- and synoptic-scales. The 12 channels consist of 7 bands near 118 GHz that measure temperature profiles of the troposphere, 3 channels near 183 GHz for water vapor profiles, a single channel near 90 GHz for imagery and precipitation measurements (when combined with the higher resolution water vapor channels), and a single channel near 205 GHz that is more sensitive to cloud-sized ice particles (Blackwell et al., 2018; 2022, 2025). An initial set of four TROPICS CubeSats successfully launched in May 2023, each with a projected lifespan of ~2 years—1 year for the primary mission and 1+ year mission extension. The CubeSats' compact design and low cost have allowed TROPICS to evolve from a scientific mission into an industry-supported initiative, with 7 additional instruments launched by a commercial partner as of June 2025 and further deployments planned.

1.02.17 ISS

The International Space Station (ISS), as shown in Fig. 3, is a laboratory for microgravity, earth, science and space research developed through an international partnership with 5 space agencies: (i) JAXA, (ii) the Canadian Space Agency (CSA), (iii) NASA, (iv) the State Corporation for Space Activities (ROSCOSMOS), and (v) the European Space Agency (ESA). It was launched in November 1998 and orbits the earth at ~400 km, with a single revolution taking roughly 93 minutes. The ISS is in a low Earth orbit (LEO) and circles between 51.6° N and 51.6° S, enabling visualization of ~75% of the earth and ~95% of its inhabited areas. The ISS is designed to house instrument payloads which can be installed on external modules and be replaced, repaired, or updated as needed. For the NASA managed research hubs, proposed payloads are reviewed by the ISS US National Lab, the Center for the Advancement of Science in Space Inc (CASIS), and the National Science Foundation (NSF). Approved projects are then assessed by the ISS Research Integration Office for compliance with available resources and technologies. US support and management of the ISS in collaboration with its international partners is projected to continue through 2030 (H R. 4346, 117th Congress (2021—2022)).

1.02.17.1 SAGE III ISS

The Stratospheric Aerosol and Gas Experiment (SAGE) III on the ISS was launched in February 2017 for a 3-year mission, and its mission was renewed in 2020 for an additional 6 years with the current end of mission date set for September 2026. SAGE III ISS uses solar occultation to measure the transmission of sunlight through the atmospheric limb during sunrise and sunset events. From these measurements, the vertical profile of aerosol optical depth, ozone, and various gaseous constituents are retrieved. The mission

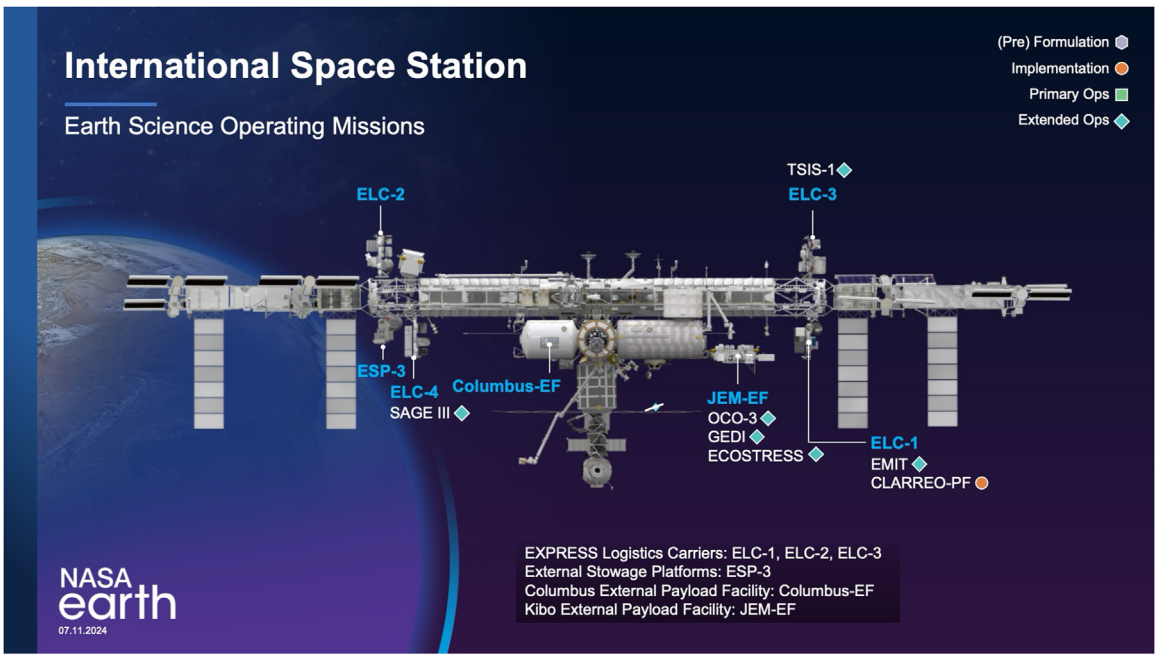


Fig. 3 Illustration of the 2024 Earth Science Operating Missions onboard the International Space Station. Credit: NASA Headquarters

Table 17 Key characteristics of the SAGE III on ISS instrument.

Instrument	*Measurement technique*	*Characteristics*
SAGE III	Grating spectrometer	809 spectral bands between 0.28 and 1.04 μm 1 spectral band at 1.55 μm Vertical resolution: 1 km

is the successor to the SAM II (1978–1993), SAGE I (1979–1981), SAGE II (1984–2005), and SAGE III Meteop-3M (M3M; 2001–2006) instruments, which observed stratospheric ozone, aerosols, and water vapor. The sensor self-calibrates as it observes an unattenuated solar disk before every sunset (or after every sunrise), and the attenuation of the radiation through the thicker layers of the atmosphere along the limb as the sun sets (or rises) allows direct inferences of atmospheric extinction. The SAGE III sensor also has the capability to measure atmospheric radiation during moonrises and moonsets, as long as the Moon's phase is greater than a quarter Moon. Lunar measurements are used primarily for ozone, nitrogen dioxide, and nitrogen trioxide inferences. Additionally, by scanning the bright side of the Earth's atmosphere after a sunrise it is capable of measuring limb scattering. From the ISS orbit, SAGE III ISS observes ~30 sunrises or sunsets each day (moonrise and moonset measurements are variable depending on the lunar phase). Characteristics of the SAGE III instrument are summarized in **Table 17**.

The SAGE III instrument consists of three major subsystems: (i) a pointing system, (ii) an imaging subsystem, and (iii) a grating spectrometer. The scan mirror scans the instrument boresight vertically across the Sun through the Earth's limb during sunrise and sunset events. The scan mirror is mounted to an azimuth drive that allows it to rotate in the azimuthal direction through 377° in order to acquire the target. The imaging subsystem consists of an f/4 Dall-Kirkham telescope, which focuses the image onto the 0.5 × 5.0 arcmin science slit. Light that passes through the science slit enters a grating spectrometer that disperses the radiation into a spectrum from 280 to 1040 nm in the first order onto a silicon CCD array with a field flattener and order sorting filters. A separate InGaAs photodiode measured radiation at 1550 nm in the zero order.

SAGE III and its predecessors SAGE III M3M and SAGE II measurements have been used for studies of (i) aerosol extinction profiles, including the effects of volcanic eruptions (Thomason and Taha, 2003; Thomason et al., 2021; Trepte et al., 1993), (ii) wildfire smoke (Lee et al., 2023; Solomon et al., 2022), (iii) ozone profiles (Bognar et al. 2022; Polyakov et al., 2005), (iii) nitrogen dioxide profiles (Dubé et al. 2022; Polyakov et al., 2005), and (iv) water vapor profiles (Park et al., 2021; Taha et al., 2004).

1.02.17.2 TSIS-1

The Total and Spectral Solar Irradiance Sensor 1 (TSIS-1), launched in December 2017 and operational since March 2018, is mounted aboard the International Space Station ExPRESS Logistics Carrier-3 atop a Three Axis Deployment system. TSIS-1 houses two instruments: (i) the Total Irradiance Monitor (TIM) which measures the Total Solar Irradiance (TSI), the amount of solar energy that reaches the outer boundaries of the Earth's atmosphere, and (ii) the Spectral Irradiance Monitor (SIM) which measures the Solar Spectral Irradiance (SSI), the amount of solar energy that reaches the outer boundaries of the Earth's atmosphere at specific wavelengths. The TIM measures TSI with an estimated uncertainty of 160 ppm and relative changes in solar irradiance within 10 ppm/yr, allowing for the identification and monitoring of long-term variations in solar irradiance. The SIM measures the solar spectral irradiance (SSI) between 200 and 2400 nm (96% of the TSI) with a spectral resolution that varies between 0.25 and 41 nm, achieving overall uncertainties at 0.42% and as low as 0.24% for certain wavelengths. In its measurement of TSI, TSIS-1 is contributing to the longest continuous space-based climate record, as TSI has been recorded since 1978. The instrument specifications for the SIM and TSI are shown in **Table 18**. This solar irradiance data collected by TSIS-1 and heritage instruments is key for understanding Earth's energy balance, assessing climate variations, and supporting accurate atmospheric measurements (Richard et al., 2024; IPCC, 2023).

Table 18 Key characteristics of the TSIS-1 instrument.

Instrument	*Measurement technique*	*Characteristics*
TIM	Ambient temperature active cavity radiometer	4 Electrical substitution radiometers (ESRs) 4 measurements/day Estimated absolute accuracy of 100 ppm (0.01%)
SIM	3-Channel solar spectral radiometer	10 spectral bands 200 nm to 2400 nm Spectral resolution: 1 nm–35 nm

1.02.17.3 ECOSTRESS

The ECOsystem Spaceborne Thermal Radiometer Experiment on Space Station (ECOSTRESS) is a thermal infrared radiometer that was mounted on the Japanese Experiment Module—Exposed Facility (JEM-EF) on the ISS in 2018. The mission measures Earth surface temperature with a swath width of 384 km and a spatial resolution of 38 m in-track by 69 m cross-track at nadir. The data is resampled to 70 × 70 m grid cells for noise reduction, and has overpass return times which vary between sub-one and five days depending on the ISS orbit. ECOSTRESS hosts the Prototype HyspIRI Thermal Infrared Radiometer (PHyTIR) built by JPL and originally developed under the Earth Science Technology Office (ESTO) Instrument Incubator Program (IIP). It has 5 thermal infrared (TIR) bands between 800 and 1250 nm and a sixth SWIR band at 1600 nm used for geolocation and cloud detection (**Table 19**). In May 2019, mass storage unit anomalies led to a shift in data acquisition strategy such that only three spectral bands were recorded. However, retrieval of all 5 bands was resumed in May of 2023.

The thermal infrared bands are used to measure the thermal properties of vegetation and man-made surfaces with a wide range of applications, including agriculture and water resource management, urban heat island dynamics, ecosystem research, and climate modeling. The mission has three main science objectives: (i) identify the critical thresholds of water use and water stress in key climate-sensitive biomes; (ii) detect the timing, location, and predictive factors leading to plant water uptake decline and/or cessation over the diurnal cycle; and (iii) measure agricultural water consumptive use over CONUS at spatiotemporal scales that can improve drought estimation accuracy (Anderson et al., 2020; Li et al., 2021; Liu et al., 2021). While the primary objectives of the mission relate to vegetation and water resources, ECOSTRESS has also been used to study volcanoes, wildfires (Puolos et al., 2021; Silvestri et al., 2020), and the impact of heat waves on urban environments (Chang et al., 2022; Pascolini-Campbell et. al., 2022). ECOSTRESS was initially scheduled for a one-year mission (2019—2020), but has been operational since and is scheduled for senior review in 2026.

1.02.17.4 GEDI

The Global Ecosystem Dynamics Investigation (GEDI) is housed on the Japanese Experiment Module − Exposed Facility (JEM-EF) of the ISS and is a joint mission between NASA and the University of Maryland. It was launched in December 2018 and passed its commissioning period in March of 2019. Originally scheduled for a two-year mission, its mission was extended through March 2023. It was then temporarily stowed before being reinstalled in April 2024. GEDI uses a full waveform LiDAR (Light Detection And Ranging) instrument to record three-dimensional elevation profiles of vegetation canopies and underlying topography. LiDAR is an active sensing technology which sends pulses of light from the instrument and records the time and intensity of their return after reflectance from the Earth's surface. These measures are used to detect the distance of objects from the sensor, and the recorded waveform of reflected energy is used to derive the elevation profiles of intercepted objects. GEDI houses 3 lasers with 56 μrad beam divergence, resulting in ground footprints of roughly 25 m in diameter. Two of the beams send pulses at full power while the third is split into two coverage (lower power) beams. The four beams are dithered through Bean Dithering Units (BDUs), resulting in 8 footprints spaced 600 m cross-track in a 4.2 km swath. The lasers operate at a 1064 nm wavelength with a beam power output between 10 and 17 mJ and a pulse rate of 242 pulses per second, resulting in 60 m along-track footprint spacing (**Table 20**). The instrument collects data between 51.6° N and 51.6° S latitudes and can be rotated up to 6° on the JEM-EF to enable lasers to be pointed up to 40 km of either side of its ground track. GEDI's orbit and design specifications allows it to see nearly all tropical and temperate forests. The measurements of structure captured by GEDI support the mission science objectives of quantifying aboveground carbon distributions (i.e., within vegetation aboveground biomass), and improving our understanding of how

Table 19 Key characteristics of the ECOSTRESS instrument.

Instrument	*Measurement technique*	*Characteristics*
PHyTIR	Thermal radiometer	6 spectral bands 8.0—12.50 μm Spatial resolution: 69 m × 38 m Swath width 385 km

Table 20 Key characteristics of the GEDI instrument.

Instrument	*Measurement technique*	*Characteristics*
GEDI	Light detection and ranging (lidar)	Lidar beam at 1064 nm Beam power: 10 mJ Spatial resolution: ~25 m Pulse rate: 242/second Pulse length: 14 ns

land surfaces and vegetation structure support ecosystem stability, biodiversity, and greenhouse gas mitigation (Dubayah et al., 2022; Potapov et al., 2021; Schneider et al., 2020; Liu et al., 2021; Duncan et al., 2016; Hunka et al., 2024; Li et al., 2024).

1.02.17.5 OCO-3

Orbiting Carbon Observatory 3 (OCO-3) was designed and built by JPL and installed on the ISS JEM-EF in 2019. It is a cost-efficient mission built using the spare hardware from OCO-2 and measures the dry-air mole fraction of carbon dioxide in the atmosphere (XCO_2) as well as the Solar-Induced chlorophyll Fluorescence (SIF) of vegetation to track the "breathing" of the planet. Much like OCO-2, it uses a 3-channel grating spectrometer configured with: (i) an oxygen A band centered at 760 nm (O2A), (ii) a weak carbon dioxide band centered at 1610 nm (weak CO_2), and (iii) a strong carbon dioxide band centered at 2060 nm (strong CO_2). The specific bands specifications are shown in **Table 21**. Unlike OCO-2, however, its position on the ISS means the local satellite overpass time varies by location. This variation enables the instrument to capture observations at different times of the day, thus allowing scientists and researchers to study the diurnal cycles in the carbon cycle and SIF signal over time. OCO-3 operates in 4 capture modes: (i) nadir mode over land; (ii) glint mode over large water bodies, (iii) targeted observations, and (iv) a novel Snapshot Area Mapping (SAM) mode. For the latter mode of operation, the fore-optics of the OCO-3 were updated with a more advanced onboard electronics control system and a two-axis pointing mirror assembly (PMA), which enables more rapid, precise, and flexible targeting from the ISS (Eldering et al., 2017). In the SAM mode, OCO-3 can capture contiguous footprints over an area as large as ~80 by 80 km^2, which have proved to be a pathfinder for studying the carbon cycle at sub-regional, city and local scales. Both these unique capabilities—capturing information about the diurnal cycle and the SAM mode observations—are unique to OCO-3. No other space-based mission, national or international, provides this type of information. Excellent instrument performance throughout the mission lifetime has provided the scientific and applications community with very high-quality and stable data products. OCO-3 data have now been used to better quantify CO_2 emissions from power plants (Nassar et al., 2022; Hakkarainen et al., 2024; Cusworth et al., 2023; Nelson et al., 2024; Moeini et al., 2025), urban areas and megacities (Kiel et al., 2021; Yang et al., 2023; Roten et al., 2023; Che et al., 2024; Hamilton et al., 2024; Jia and Li, 2025; Ahn et al., 2025). In addition, studies have leveraged the diurnal SIF measurements from OCO-3 to obtain insights into plant health, their response to droughts and their diurnal water-use efficiency (Zhang et al., 2023, Zhang et al., 2023, Liu et al., 2024a, b; Deng et al., 2025) and volcanoes (Romaniello and Ganci, 2025). Being on the ISS, OCO-3 observations are used synergistically with information from other ISS instruments, such as EMIT for monitoring anthropogenic emissions (Nelson et al., 2024) and ECOSTRESS for studying how plant functioning and ecosystem processes vary over the course of the diurnal cycle (Xiao et al., 2021).

OCO-2 and OCO-3 have been successfully used to better understand the carbon cycle at global (Crowell et al., 2019; Peiro et al., 2022; Byrne et al., 2023), regional (Palmer et al., 2019; Philip et al., 2022; Feldman et al., 2023), urban (Kiel et al., 2021; Roten et al., 2023) and even facility scales (Nassar et al., 2022; Moeini et al., 2025). If OCO-2 and OCO-3 continue to operate concurrently, their complementary sampling will continue to provide new insights into the sources and sinks of carbon dioxide at unprecedented spatial and temporal scales—scales that have not been possible from space before.

1.02.17.6 EMIT

The NASA Earth Surface Mineral Dust Source Investigation (EMIT) mission was launched to the ISS in 2022 and is designed to measure the composition and sources of mineral-dust using the unique spectral signatures of light reflected by different materials. EMIT uses an advanced Dyson imaging spectrometer designed for high spatial and spectral resolution with minimal distortions in the field of view (Green et al., 2020, 2024). The spectrometer records 285 visible and infrared wavelengths between 380−2500 nm at a spectral sampling resolution of 7.5 nm. EMIT has demonstrated exceptionally performance, with a spectral uniformity greater than 98% and a signal-to-noise ratio (SNR) ranging from 500 to 750 for most wavelengths at the US Geological Survey (USGS) Libya 4 calibration site (Thompson et al., 2024). The pushbroom imager spectrometer has a swath width of 80 km, a pixel resolution of roughly 60 m (**Table 22**). The ISS orbit enables EMIT to capture most of the significant sources of dust globally, which are concentrated in arid and semi-arid regions and include major deserts such as the Sahara in Africa, the Gobi in Asia, and the Arabian Desert in the Middle East.

The measurements from EMIT provide insight into the regional differences in dust composition and their impact on the Earth's energy balances and biogeochemical cycles. The dust cycle, which describes the generation, suspension, transport, and deposition of

Table 21 Key characteristics of the OCO-3 instrument.

Instrument	*Measurement technique*	*Characteristics*
OCO-3	3 long-slit imaging grating spectrometers	3 NIR bands (0.76−0.77, 1.59−1.62, 2.04−2.08 μm) Spectral resolution: (0.04, 0.08, 0.10 nm) Spatial resolution: 1.29 × 2.25 km Swath width: 10 km

Table 22 Key characteristics of the EMIT instrument.

Instrument	*Measurement technique*	*Characteristics*
EMIT	Advanced Dyson imaging spectrometer	285 spectral bands Spectral range: 380–2500 nm Spectral resolution: 7.5 nm Swath width: 80 km Spatial sampling: 60 m

mineral dust, plays an important role in Earth System Models and is a large source of uncertainty in aerosol radiative forcing quantification. EMIT achieved its prime mission objectives in 2024.

EMIT full imaging spectroscopy observations are now being used to deliver new value to our nation with mineral mapping (rare earths, lithium, etc.), wildfire fuel characterization (species-type, canopy water, burnable and non-burnable material, etc.), precision agriculture, forestry, water quality, aquaculture, water resources, national interests, and more.

1.02.18 Summary and Conclusion

Through the development of multiple spacecraft and Earth-viewing instruments aimed at improving our understanding of our changing planet, the NASA ESD has enabled critical contributions to the understanding of our inhabited planet and the study of Earth system science.

The transition from the EOS era, characterized by the Terra, Aqua, and Aura flagship satellites, to the JPSS era, marked by the Suomi-NPP and subsequent NOAA polar-orbiting satellites, represents a significant evolution in Earth observation capabilities. In land imaging, Román et al. (2024) highlight the concerted efforts to harmonize MODIS and VIIRS data products, ensuring that long-term Earth System Data Records remain uninterrupted. This seamless integration supports a wide array of applications, from long-term studies to disaster response. The continued development of the JPSS program — with current satellites Suomi NPP, NOAA-20, and NOAA-21, and future missions NOAA-22 and NOAA-23 — ensures the legacy of Terra, Aqua, Aura, and the EOS program, delivering consistent, high-quality data to scientists, stakeholders, and decision-makers.

Looking forward, NASA is looking to embark on the next era of earth observation systems with the Earth System Observatory (ESO), a collection of satellites that will provide key information in understanding Earth's climate, hazards, ecosystems, and resources. Working from recommendations in the 2017 Earth Science Decadal Study (National Academies of Science, 2017), the new suite of sensors will focus on 5 core elements: (i) aerosols; (ii) cloud, convention and precipitation; (iii) mass change; (iv) surface biology and geology; and (v) surface deformation and change.

Acknowledgements

The authors would like to thank the many members, past and present, of the EOS and ESD instrument, calibration and science teams who have contributed so much to our understanding of Earth system science. We would also like to thank Steve Platnick and Michael King, the authors of the first edition of this chapter, for their continued support of Earth Science missions and leadership in the field of Earth observations. Additionally, we would like to thank William Blackwell, Scott Braun, Abhishek Chatterjee, Bryan Duncan, Denis Felikson, David Flittner, Lee-Lueng Fu, Robert O. Green, Michelle Hofton, Felix W. Landerer, Xiong Liu, Christopher Neigh, Lazaros Oreopoulos, Chris Ruf, Adam Szabo and Dong Wu for their feedback and input on select sections of this text.

References

Abrams, M., et al., 2015. The advanced spaceborne thermal emission and reflection radiometer (ASTER) after fifteen years: review of global products. Int. J. Appl. Earth Obs. Geoinf. 38, 292–301.

Adirosi, E., et al., 2016. Improvement of vertical profiles of raindrop size distribution from micro rain radar using 2D video disdrometer measurements. Atmos. Res. 169, 404–415.

Ahn, D.Y., et al., 2025. Satellite-based analysis of CO_2 emissions from global cities: regional, economic, and demographic attributes. AGU Adv. 6, e2025AV001747.

Alizadeh, M.R., et al., 2024. Land and atmosphere precursors to fuel loading, wildfire ignition and post-fire recovery. Geophys. Res. Lett. 51, e2023GL105324.

Anderson, et al., 2020. Interoperability of ECOSTRESS and Landsat for mapping evapotranspiration time series at sub-field scales. Rem. Sens. Environ. 252.

Asanuma, I., et al., 2016. Detection limit of fishing boats by the day night band (DNB) on VIIRS. International Society for Optics and Photonics, 99760P–99760P–8.

Aumann, H.H., et al., 2003. AIRS/AMSU/HSB on the Aqua mission: design, science objectives, data products, and processing systems. IEEE Trans. Geosci. Rem. Sens. 41, 253–264.

Babbel, B.J., et al., 2021. ICESat-2 elevation retrievals in support of satellite-derived bathymetry for global science applications. Geophys. Res. Lett. 48.

Beer, R., 2006. TES on the Aura mission: scientific objectives, measurements, and analysis overview. IEEE Trans. Geosci. Rem. Sens. 44, 1102–1105.

Blackwell, W.J., et al., 2018. An overview of the TROPICS NASA earth venture mission. Q. J. R. Meteorol. Soc. 144, 16–26.

Blackwell, W.J., et al., 2022. On-orbit results from the NASA TROPICS mission. Proc. SPIE 12236, CubeSats and SmallSats for Remote Sensing VI, 122360.
Blackwell, W., et al., 2025. Tropical cyclone observations using a CubeSat constellation: recent results from the NASA TROPICS Mission. In: Proc. SPIE 13546, Small Satellites Systems and Services Symposium (4S 2024).
Bognar, K., et al., 2022. Stratospheric ozone trends for 1984–2021 in the SAGE II–OSIRIS–SAGE III/ISS composite dataset. Atmos. Chem. Phys. 22, 9553–9569.
Buzzanga, B., et al., 2021. An assessment of regional ICESat-2 sea-level trends. Geophys. Res. Lett. 48.
Byrne, B., et al., 2021. The carbon cycle of southeast Australia during 2019–2020: drought, fires, and subsequent recovery. AGU Advances 2, e2021AV000469.
Byrne, B., et al., 2023. National CO2 budgets (2015–2020) inferred from atmospheric CO2 observations in support of the global stocktake. Earth Syst. Sci. Data 15, 963–1004.
Carr, J.L., et al., 2024. TEMPO at Night. ESS Open Archive.
Carreno-Luengo, H., Crespo, J.A., Akbar, R., Bringer, A., Warnock, A., Morris, M., Ruf, C., 2021. The CYGNSS mission: on-going science team investigations. Remote Sens. 13 (9), 1814.
Carreno-Luengo, et al., 2024. Detection of inland water bodies under dense biomass by CYGNSS. Rem. Sens. Environ. 301.
Chahine, M.T., et al., 2006. Improving weather forecasting and providing new data on greenhouse gases. Bull. Am. Meteorol. Soc. 87, 911–926.
Chahine, M.T., et al., 2008. Satellite remote sounding of mid-tropospheric CO2. Geophys. Res. Lett. 35, L17807.
Chang, L., Sun, W., 2022. Consistency analysis of GRACE and GRACE-FO data in the study of global mean sea level change. Geodesy and Geodynamics 13.
Chang, et al., 2022. Combining GOES-R and ECOSTRESS land surface temperature data to investigate diurnal variations of surface urban heat island. Sci. Total Environ. 823.
Chatterjee, A., et al., 2017. Influence of El Niño on atmospheric CO2 over the tropical pacific ocean: findings from NASA's OCO-2 mission. Science 358, 6360.
Che, K., et al., 2024. Urban XCO2 gradients from a dense network of solar absorption spectrometers and OCO-3 over Mexico City. J. Geophys. Res. Atmos. 129, e2023JD040063.
Chen, J., et al., 2022. Applications and challenges of GRACE and GRACE follow-on satellite gravimetry. Surv. Geophys. 43, 305–345.
Ciracì, E., Velicogna, I., Swenson, S., 2020. Continuity of the mass loss of the world's glaciers and ice caps from the GRACE and GRACE Follow-On missions. Geophys. Res. Lett. 47.
Colle, B.A., Naeger, A.R., Molthan, A., 2017. Structure and evolution of a warm frontal precipitation band during the GPM cold season precipitation experiment (GCPEx). Mon. Weather Rev. 145, 473–493.
Colliander, A., et al., 2020. SMAP detects soil moisture under temperate forest canopies. Geophys. Res. Lett. 47, e2020GL089697.
Comiso, J., Hall, D., 2014. Climate trends in the Arctic as observed from space. Clim. Change 5, 389–409.
Comiso, J.C., et al., 2008. Accelerated decline in the Arctic Sea ice cover. Geophys. Res. Lett. 35.
Crisp, D., et al., 2017. The on-orbit performance of the Orbiting Carbon Observatory-2 (OCO-2) instrument and its radiometrically calibrated products. Atmos. Meas. Tech. 10, 59–81
Crisp, D., Miller, C.E., DeCola, P.L., 2008. NASA Orbiting Carbon Observatory: measuring the column averaged carbon dioxide mole fraction from space. J. Appl. Remote Sens. 2, 023508.
Crowell, S., et al., 2019. The 2015–2016 carbon cycle as seen from OCO-2 and the global in situ network. Atmos. Chem. Phys. 19, 9797–9831.
Cusworth, D.H., et al., 2023. Two years of satellite-based carbon dioxide emission quantification at the world's largest coal-fired power plants. Atmos. Chem. Phys. 23, 14577–14591.
Das, S., et al., 2025. Comparisons of the v11.1 Orbiting Carbon Observatory-2 (OCO-2) XCO2 measurements with GGG2020 TCCON. Earth Space Sci. 12, e2024EA003935.
Deeter, M.N., et al., 2014. The MOPITT Version 6 product: algorithm enhancements and validation. Atmos. Meas. Tech. 7, 3623–3632.
Deng, Z., et al., 2025. Response of vegetation photosynthesis to the 2022 drought in yangtze river basin by diurnal orbiting carbon observatory-2/3 satellite observations. J Remote Sens 5, 0445.
Doughty, R., et al., 2021. Small anomalies in dry-season greenness and chlorophyll fluorescence for Amazon moist tropical forests during El Niño and La Niña Rem. Sens. Environ 253, 112196.
Dubayah, R., et al., 2022. GEDI launches a new era of biomass inference from space. Environ. Res. Lett. 17.
Dubé, K., et al., 2022. Tropopause-level NOx in the Asian summer monsoon. Geophys. Res. Lett. 49, e2022GL099848.
Duncan, B.N., et al., 2016. A space-based, high-resolution view of notable changes in urban NOx pollution around the world (2005–2014). J. Geophys. Res. 121, 976–996.
Eldering, A., et al., 2017. The Orbiting Carbon Observatory-2 early science investigations of regional carbon dioxide fluxes. Science 358 (6360), eaam5745.
Elvidge, C., et al., 2015. Methods for global survey of natural gas flaring from visible infrared imaging radiometer suite data. Energies 9, 14.
Endsley, K., et al., 2020. Satellite monitoring of global surface soil organic carbon dynamics using the SMAP Level 4 Carbon product. J. Geophys. Res.: Biogeosciences 125, e2020JG006100.
Feldman, A.F., et al., 2023. A multi-satellite framework to rapidly evaluate extreme biosphere cascades: the Western US 2021 drought and heatwave. Glob. Change Biol. 29, 3634–3651.
Feldman, A., et al., 2024. Large global-scale vegetation sensitivity to daily rainfall variability. Nature 636, 380–384.
Friedl, M.A., et al., 2010. MODIS Collection 5 global land cover: algorithm refinements and characterization of new datasets. Rem. Sens. Environ. 114, 168–182.
Fu, L.L., et al., 2024. The Surface Water and Ocean Topography Mission: a breakthrough in radar remote sensing of the ocean and land surface water. Geophys. Res. Lett. 51, e2023GL107652.
Gentemann, C.L., Meissner, T., Wentz, F.J., 2010. Accuracy of satellite sea surface temperatures at 7 and 11 GHz. IEEE Trans. Geosci. Rem. Sens. 48, 1009–1018.
Ghobadi-Far, K., et al., 2020. GRACE Follow-On laser ranging interferometer measurements uniquely distinguish short-wavelength gravitational perturbations. Geophys. Res. Lett. 47, e2020GL089445.
Giglio, L., Randerson, J.T., van der Werf, G.R., 2013. Analysis of daily, monthly, and annual burned area using the fourth-generation global fire emissions database (GFED4). J. Geophys. Res. 118, 317–328.
Gille, J., et al., 2005. Development of special corrective processing of HIRDLS data, and early validation. Proc. SPIE 5883, H1–H11.
Goffin, B.D., et al., 2024. Mapping extreme wildfires using a critical threshold in SMAP soil moisture. Remote Sens. 16, 2457.
Goward SN, et al. (in press) *Landsat's Enduring Legacy: Pioneering Global Land Observations from Space.* Bethesda: American Society of Photogrammetry and Remote Sensing.
Green, R.O., et al., 2020. The Earth surface mineral dust source investigation: an Earth science imaging spectroscopy mission. In: 2020 IEEE Aerospace Conference. IEEE.
Green, R.O., et al., 2024. Performance and early results from the Earth surface mineral dust source investigation (EMIT) imaging spectroscopy mission. In: 2023 IEEE Aerospace Conference. IEEE, 2023.
Haines, B., et al., 2024. A global combination of geodetic techniques at the observation level: new perspectives on the terrestrial reference frame. J. Geophys. Res. Solid Earth 129, e2024JB029527.
Hakkarainen, J., et al., 2024. Building a bridge: characterizing major anthropogenic point sources in the South African Highveld region using OCO-3 carbon dioxide snapshot area maps and Sentinel-5P/TROPOMI nitrogen dioxide columns. Environ. Res. Lett. 3, 18.
Hall, D.K., et al., 2010. Development and evaluation of a cloud-gap-filled MODIS daily snow-cover product. Rem. Sens. Environ. 114, 496–503.
Hamilton, S.D., et al., 2024. Estimating carbon dioxide emissions in two California cities using Bayesian inversion and satellite measurements. Geophys. Res. Lett. 51, e2024GL111150.

Han, Y., et al., 2013. Suomi NPP CrIS measurements, sensor data record algorithm, calibration and validation activities, and record data quality. J. Geophys. Res. Atmos. 118, 12,734–12,748.
Hao, D., et al., 2020. DSCOVR/EPIC-derived global hourly and daily downward shortwave and photosynthetically active radiation data at 0.1° × 0.1° resolution. Earth Syst. Sci. Data 12, 2209–2221.
Herzfeld, U., et al., 2021. Detection and height measurement of tenuous clouds and blowing snow in ICESat-2 ATLAS data. Geophys. Res. Lett. 48, e2021GL093473.
Hu, Y., Shi, Y., 2021. Estimating CO2 emissions from large scale coal-fired power plants using OCO-2 observations and emission inventories. Atmosphere 12 (7), 811.
Huffman, G.J., et al., 2015. NASA global precipitation measurement (GPM) integrated multi-satellite retrievals for GPM (IMERG). Algorithm Theoretical Basis Document (ATBD) Version 4, 26.
Hunka, N., et al., 2024. Intergovernmental panel on climate change (IPCC) tier 1 forest biomass estimates from earth observation. Sci. Data 11, 1127.
IPCC, 2023. Climate change 2023: synthesis report. In: Lee, H., Romero, J. (Eds.), Contribution of Working Groups I, II and III to the Sixth Assessment Report of the Intergovernmental Panel on Climate Change [Core Writing Team. IPCC, Geneva, Switzerland, p. 184.
Irons, J.R., Dwyer, J.L., Barsi, J.A., 2012. The next Landsat satellite: the Landsat data continuity mission. Rem. Sens. Environ 122, 11–21.
Jia, M., Li, Y., et al., 2025. Spatial distribution of urban anthropogenic carbon emissions revealed from the OCO-3 snapshot XCO2 observations: a case study of shanghai. Remote Sens. 17 (6), 1087.
Jiang, X., et al., 2021. Impact of Amazonian fires on atmospheric CO2. Geophys. Res. Lett. 48, e2020GL091875.
Johnson, R.S., et al., 2013. Preliminary investigations toward nighttime aerosol optical depth retrievals from the VIIRS day/night band. Atmos.
Joint Polar Satellite System (JPPS) VIIRS Geolocation Algorithm Theoretical Basis Document (ATBD), Document Number: 474-00053, Version B, Effective Date, 2011.
Kadrolli, V., Kalnoor, G., 2024. AI-infused strategies for mitigating uncertainty in continental-scale surface mass change analysis through GPS and GRACE-FO. Remote Sens. Earth Syst. Sci. 7, 80–89.
Kahn, B.H., et al., 2014. The Atmospheric Infrared Sounder version 6 cloud products. Atmos. Chem. Phys. 14, 399–426.
Kiel, M., et al., 2021. Urban-focused satellite CO2 observations from the orbiting carbon observatory-3: a first look at the Los Angeles megacity. Remote Sens. Environ. 258.
Kilpatrick, K.A., et al., 2015. A decade of sea surface temperature from MODIS. Rem. Sens. Environ. 165, 27–41.
Kim, Y., et al., 2023. Global estimates of daily evapotranspiration using SMAP surface and root-zone soil moisture. Rem. Sens. Environ. 298, 113803.
King, M.D., et al., 2003. Cloud and aerosol properties, precipitable water, and profiles of temperature and water vapor from MODIS. IEEE Trans. Geosci. Rem. Sens. 41, 442–458.
King, M.D., et al., 2013. Spatial and temporal distribution of clouds observed by MODIS onboard the Terra and Aqua satellites. IEEE Trans. Geosci. Rem. Sens. 51, 3826–3852.
Kirschbaum, D., et al., 2017. NASA's remotely-sensed precipitation: a reservoir for applications users. Bull. Am. Meteorol. Soc. 98, 1169–1184.
Kornfeld, R.P., et al., 2019. GRACE-FO: the gravity recovery and climate experiment follow-on mission. J. Spacecraft Rockets 56 (3), 931–951.
Laipelt, L., et al., 2025. SWOT reveals how the 2024 disastrous flood in South Brazil was intensified by increased water slope and wind forcing. Geophys. Res. Lett. 52, e2024GL111287.
Landerer, F.W., et al., 2020. Extending the global mass change data record: GRACE Follow-On instrument and science data performance. Geophys. Res. Lett. 47, e2020GL088306.
Larnier, K., et al., 2020. River discharge and bathymetry estimation from SWOT altimetry measurements. Inverse Problems Sci. Eng. 29 (6), 759–789.
L'Ecuyer, T., Jiang, J., 2010. Touring the atmosphere aboard the A-train. Phys. Today 63, 36–41.
Lee, H.-H., Lundquist, K.A., Tang, Q., 2023. Pyrocumulonimbus events overBritish Columbia in 2017: an ensemble model study of parameter sensitivities and climate impacts of wildfire smoke in the stratosphere. J. Geophys. Res. Atmos. 128, e2022JD037648.
Levelt, P.F., et al., 2006. The ozone monitoring instrument. IEEE Trans. Geosci. Rem. Sens. 44, 1093–1101.
Levy, R.C., et al., 2013. The Collection 6 MODIS aerosol products over land and ocean. Atmos. Meas. Tech. 6, 2989–3034.
Li, et al., 2021. ECOSTRESS estimates gross primary production with fine spatial resolution for different times of day from the ISS. Rem. Sens. Environ. 258.
Li, Y., et al., 2024. Validation of the vertical canopy cover profile products derived from GEDI over selected forest sites. Rem. Sens. Environ. 137, 100158.
Liu, J.C., et al., 2009. Validation of Moderate Resolution Imaging Spectroradiometer (MODIS) albedo retrieval algorithm: dependence of albedo on solar zenith angle. J. Geophys. Res. 114.
Liu, et al., 2021. An Evaluation of ECOSTRESS Products of a Temperate Montane Humid Forest in a Complex Terrain Environment, p. 265.
Liu, Y., et al., 2024a. Atmospheric dryness dominates afternoon depression of global terrestrial photosynthesis. Geophys. Res. Lett. 51, e2024GL110954.
Liu, J., et al., 2024b. Enhanced carbon flux response to atmospheric aridity and water storage deficit during the 2015–2016 El Niño compromised carbon balance recovery in tropical South America. AGU Advances 5, e2024AV001187.
Loeb, N.G., Wielicki, B.A., 2015. Earth's radiation budget. In: North, G.R., Pyle, J., Zhang, F. (Eds.), Encyclopedia of Atmospheric Sciences, second ed, vol. 5. Elsevier, Amsterdam, pp. 67–76.
Loto'aniu, P.T.M., et al., 2022. Validation of the DSCOVR spacecraft mission space weather solar wind products. Space Weather 20, e2022SW003085.
Loveland, T.R., Irons, J.R., 2016. Landsat 8: the plans, the reality, and the legacy. Rem. Sens. Environ. 185, 1–6.
Lyapustin, A.,Y., et al., 2021. Atmospheric correction of DSCOVR EPIC: version 2 MAIAC algorithm. Frontiers in Remote Sens 2.
Markus, et al., 2017. The ice, cloud, and land elevation satellite-2 (ICESat-2): science requirements, concept, and implementation. Rem. Sens. Environ 190.
Marshak, A.,J., et al., 2018. Earth observations from DSCOVR/EPIC instrument. Bull. Am. Meteorol. Soc. 99 (9), 1829–1850.
Masek, J.G., 2020. Landsat 9: empowering open science and applications through continuity. Rem. Sens. Environ 248, 111968.
McHardy, T.M., et al., 2015. An improved method for retrieving nighttime aerosol optical thickness from the VIIRS Day/Night Band. Atmos. Meas. Tech. 8, 4773–4783.
McPeters, R.D., Frith, S., Labow, G.J., 2015. OMI total column ozone: extending the long-term data record. Atmos. Meas. Tech. 8, 4845–4850.
Minnis, P., et al., 2016. Estimating nocturnal opaque ice cloud optical depth from MODIS multispectral infrared radiances using a neural network method. J. Geophys. Res. Atmos. 121, 4907–4932.
Mladenova, et al., 2019. Evaluating the operational application of SMAP for global agricultural drought monitoring. IEEE J. Sel. Top. Appl. Earth Obs. Rem. Sens. 12 (9), 3387–3397.
Moeini, O., et al., 2025. Quantifying CO2 emissions from smaller anthropogenic point sources using OCO-2 target and OCO-3 snapshot area mapping mode observations. J. Geophys. Res. Atmos. 130, e2024JD042333.
NASA Advisory Council, 1986. Earth System Science: Overview, Report of the Earth System Sciences Committee. NASA, Washington, DC, p. 48.
NASA Advisory Council, 1988. Earth System Science: A Closer Look, Report of the Earth System Sciences Committee. NASA, Washington, DC, p. 208.
Nassar, R., et al., 2017. Quantifying CO2 emissions from individual power plants from space. Geophys. Res. Lett. 44, 10,045–10,053.
Nassar, R., et al., 2022. Tracking CO2 emission reductions from space: a case study at Europe's largest fossil fuel power plant. Front. Remote Sens. 3, 98.
National Research Council, 1985. A Strategy for Earth Science from Space in the 1980's and 1990's, Part II: Atmosphere and Interactions with the Solid Earth, Oceans, and Biota. National Academy Press, Washington, DC, p. 165.
National Research Council, 1986. Global Change in the Geosphere-Biosphere: Initial Priorities for an IGBP. National Academy Press, Washington, DC, p. 91.
National Research Council, 1988. Physical Oceanography and Tracer Chemistry of the Southern Ocean: Polar Research—A Strategy. National Academy Press, Washington, DC, p. 82.
National Research Council, 1990. One Earth One Future: Our Changing Global Environment. National Academy Press, Washington, DC, p. 196.

Nelson, R.R., et al., 2024. Comparing point source CO2 emission rate estimates from near-simultaneous OCO-3 and EMIT observations. Geophys. Res. Lett. 51.
Neuenschwander, et al., 2020. Validation of ICESat-2 terrain and canopy heights in boreal forests. Rem. Sens. Environ 251.
Palm, S.P., et al., 2021. ICESat-2 atmospheric channel description, data processing and first results. Earth Space Sci. 8.
Palmer, P.I., et al., 2019. Net carbon emissions from African biosphere dominate pan-tropical atmospheric CO2 signal. Nat. Commun. 10, 3344.
Pan, C., Weng, F., Flynn, L., 2017. Spectral performance and calibration of the Suomi NPP OMPS nadir profiler sensor. Earth Space Sci. 4, 737—745.
Pandey, S., et al., 2024. Toward low-latency estimation of atmosphericCO2 growth rates using satellite observations: evaluating sampling errors of satellite and in situ observing approaches. AGU Adv. 5, e2023AV001145.
Parazoo, N., et al., 2024. Antecedent conditions mitigate carbon loss during flash drought events. Geophys. Res. Lett. 51, e2024GL108310.
Park, M., et al., 2021. Near-global variability of stratospheric water vapor observed by SAGE III/ISS. J. Geophys. Res. Atmos. 126, e2020JD034274.
Parkinson, C.L., 2003. Aqua: an Earth-observing satellite mission to examine water and other climate variables. IEEE Trans. Geosci. Rem. Sens. 41, 173—183.
Parkinson, C.L., 2013. Summarizing the first ten years of NASA's Aqua mission. IEEE J. Sel. Top. Appl. Earth Obs. Rem. Sens. 6, 1179—1188.
Parkinson, C.L., 2022. The Earth-observing Aqua satellite mission: 20 years and counting. Earth Space Sci. 9, e2022EA002481.
Parkinson, C.L., Comiso, J.C., 2008. Antarctic sea ice parameters from AMSR-E data using two techniques and comparisons with sea ice from SSM/I. J. Geophys. Res. 113, C02S06.
Parrish, C.E., et al., 2019. Validation of ICESat-2 ATLAS bathymetry and analysis of ATLAS's bathymetric mapping performance. Remote Sens. 11 (14), 1634.
Pascolini-Campbell, et al., 2022. ECOSTRESS reveals pre-fire vegetation controls on burn severity for Southern California wildfires of 2020. Global Biol. Biogeog.
Peiro, H., et al., 2022. Four years of global carbon cycle observed from the Orbiting Carbon Observatory 2 (OCO-2) version 9 and in situ data and comparison to OCO-2 version 7, Atmos. Chem. Phys. 22, 1097—1130.
Philip, S., et al., 2022. OCO-2 satellite-imposed constraints on terrestrial biospheric CO2 fluxes over South Asia. J. Geophys. Res. Atmos. 127, e2021JD035035.
Polivka, T.N., et al., 2016. Improving nocturnal fire detection with the VIIRS day—night band. IEEE Trans. Geosci. Rem. Sens. 54, 5503—5519.
Polyakov, A.V., et al., 2005. Retrieval of ozone and nitrogen dioxide concentrations from Stratospheric Aerosol and Gas Experiment III (SAGE III) measurements using a new algorithm. J. Geophys. Res. 110.
Potapov, et al., 2021. Mapping global forest canopy height through integration of GEDI and Landsat data. Rem. Sens. Environ. 253, 112165.
Pu, Z., et al., 2019. The impact of assimilation of GPM microwave imager clear-sky radiance on numerical simulations of hurricanes joaquin (2015) and matthew (2016) with the HWRF model. Mon. Weather Rev. 147 (1), 175—198.
Puolos, et al., 2021. Wildfire severity and vegetation recovery drive post-fire evapotranspiration in a southwestern pine-oak forest, Arizona, USA. Remote Sens. Ecol. Conserv.
Purdy, A.J., et al., 2018. SMAP soil moisture improves global evapotranspiration. Rem. Sens. Environ 219, 1—14.
Rahman, M.S., et al., 2019. Rapid flood progress monitoring in cropland with NASA SMAP. Remote Sens. 11 (2), 191.
Richard, E., et al., 2024. Advancements in solar spectral irradiance measurements by the TSIS-1 spectral irradiance monitor and its role for long-term data continuity. J. Space Weather Space Clim. 14.
Román, M.O., et al., 2018. NASA's Black Marble nighttime lights product suite. Rem. Sens. Environ. 210, 113—143.
Román, M.O., et al., 2019. Satellite-based assessment of electricity restoration efforts in Puerto Rico after Hurricane Maria. PLoS One 14 (6), e0218883.
Román, M.O., et al., 2024. Continuity between NASA MODIS collection 6.1 and VIIRS collection 2 land products. Rem. Sens. Environ. 302, 113963.
Romaniello, V., Ganci, G., 2025. Exploitation of OCO-3 satellite data to analyse carbon dioxide emissions from the Mt. Etna Volcano. Remote Sens. 17 (11), 1918.
Roten, D., et al., 2023. Constraining sector-specific CO2 fluxes using space-based XCO2 observations over the Los Angeles Basin. Geophys. Res. Lett. 50, e2023GL104376.
Ryan, J.C., et al., 2020. Global characterization of inland water reservoirs using ICESat-2 altimetry and climate reanalysis. Geophys. Res. Lett. 47, e2020GL088543.
Santi, et al., 2020. Soil moisture and forest biomass retrieval on a global scale by using CyGNSS data and artificial neural networks. In: 2020 IEEE International Geoscience and Remote Sensing Symposium, Waikoloa, HI, USA, pp. 5905—5908.
Schneider, et al., 2020. Towards mapping the diversity of canopy structure from space with GEDI. Environ. Res. Lett. 15.
Schoeberl, M.R., et al., 2006. Overview of the EOS Aura mission. IEEE Trans. Geosci. Rem. Sens. 44, 1066—1074.
Schumann, G.J.-P., et al., 2016. Unlocking the full potential of Earth observation during the 2015 Texas flood disaster. Water Resour. Res. 52, 3288—3293.
Schutz, B.E., et al., 2005. Overview of the ICESat mission. Geophys. Res. Lett. 32, L21S01.
Silvestri, et al., 2020. First comparisons of surface temperature estimations between ECOSTRESS, ASTER and Landsat 8 over Italian volcanic and geothermal areas. Remote Sens.
Smith, L.C., et al., 2023. Peace-Athabasca Delta water surface elevations and slopes mapped from AirSWOT Ka-band InSAR. Remote Sens. Lett. 14 (12), 1238—1250.
Solomon, S., et al., 2022. On the stratospheric chemistry of midlatitude wildfire smoke. Proc. Natl. Acad. Sci. U.S.A. 119 (10), e2117325119.
Srinivasan, M., Tsontos, V., 2023. Satellite altimetry for ocean and coastal applications: a review. Remote Sens. 15 (16), 3939.
Su, W., et al., 2020. Determining the daytime earth radiative flux from national Institute of standards and technology advanced radiometer (NISTAR) measurements. Atmos. Meas. Tech. 13, 429—443.
Sun, J., et al., 2022. The Sea level fingerprints of global terrestrial water storage changes detected by GRACE and GRACE-FO data. Pure Appl. Geophys. 179, 3493—3509.
Taha, G., Thomason, L.W., Burton, S.P., 2004. Comparison of Stratospheric Aerosol and Gas Experiment (SAGE) II version 6.2 water vapor with balloon-borne and space-based instruments. J. Geophys. Res. 109, D18313.
Tanaka, Y., 2023. Coseismic gravity changes and crustal deformation induced by the 2018 Fiji deep-focus earthquake observed by GRACE and GRACE-FO satellites. Remote Sens. 15 (2), 495.
Tapiador, F.J., et al., 2017. Global precipitation measurements for validating climate models. Atmos. Res. 197, 1—20.
Thomason, L.W., Taha, G., 2003. SAGE III aerosol extinction measurements: initial results. Geophys. Res. Lett. 30 (12).
Thomason, L.W., et al., 2021. Evidence for the predictability of changes in the stratospheric aerosol size following volcanic eruptions of diverse magnitudes using space-based instruments. Atmos. Chem. Phys. 21, 1143—1158.
Thompson, et al., 2024. On-orbit calibration and performance of the EMIT imaging spectrometer. Remote Sens. Environ.
Tobin, D., et al., 2013. Suomi-NPP CrIS radiometric calibration uncertainty. J. Geophys. Res. Atmos. 118, 10,589—10,600.
Torres, O., et al., 2007. Aerosols and surface UV products from Ozone Monitoring Instrument observations: an overview. J. Geophys. Res. 112, D24S47.
Trepte, C.R., Veiga, R.E., McCormick, M.P., 1993. The poleward dispersal of Mount Pinatubo volcanic aerosol. J. Geophys. Res. 98, 18563—18573.
Varnai, T., Marshak, A., Kostinski, A., 2021. Operational detection of sun glints in DSCOVR EPIC images. Front. Remote Sens. 2.
Velicogna, I., et al., 2020. Continuity of ice sheet mass loss in Greenland and Antarctica from the GRACE and GRACE Follow-On missions. Geophys. Res. Lett. 47, e2020GL087291.
Verma, M., et al., 2014. Remote sensing of annual terrestrial gross primary productivity from MODIS: an assessment using the FLUXNET La Thuile data set. Biogeosciences 11, 2185—2200.
Walker, E., et al., 2019. Regional evapotranspiration estimates using the relative soil moisture ratio derived from SMAP products. Agric. Water Manag. 216, 254—263.
Walther, A., et al., 2013. The expected performance of cloud optical and microphysical properties derived from soumi NPP VIIRS day/night band lunar reflectance. J. Geophys. Res. Atmos. 2013JD020478.
Wang, J., et al., 2016. Potential application of VIIRS Day/Night Band for monitoring nighttime surface PM 2.5 air quality from space. Atmos. Environ. 124, 55—63.
Wang, Z., et al., 2018. NASA's black marble product suite: validation strategy. IGARSS 2018 - 2018. IEEE Int. Geosci. Remote Sens. Symposium 8197—8200.

Waters, J.W., et al., 2006. The earth observing system microwave limb sounder (EOS MLS) on the Aura satellite. IEEE Trans. Geosci. Rem. Sens. 44, 1075–1092.
Wilmot, T.Y., et al., 2024. Toward a satellite-based monitoring system for urban CO2 emissions in support of global collective climate mitigation actions. Environ. Res. Lett. 19 (8), 084029.
Wu, H., et al., 2014. Real-time global flood estimation using satellite-based precipitation and a coupled land surface and routing model. Water Resour. Res. 50, 2693–2717.
Wu, D., et al., 2020. Space-based quantification of per capita CO2 emissions from cities. Environ. Res. Lett. 15 (3), 035004.
Wulder, et al., 2019. Current status of Landsat program, science, and applications. Rem. Sens. Environ. 225.
Wulder, et al., 2022. Fifty years of Landsat science and impacts. Rem. Sens. Environ. 280.
Xiao, J., et al., 2021. Emerging satellite observations for diurnal cycling of ecosystem processes. Nat. Plants 7, 877–887.
Xiong, X., et al., 2016. Moderate resolution imaging spectroradiometer (MODIS) on Terra and Aqua missions. In: Qian, S.E. (Ed.), Optical Payloads for Space Missions, 1e. Wiley, Singapore, pp. 53–89.
Xu, X., et al., 2017. Passive remote sensing of altitude and optical depth of dust plumes using the oxygen A and B bands: first results from EPIC/DSCOVR at Lagrange-1 point. Geophys. Res. Lett. 44, 7544–7554.
Yang, K., et al., 2013. First observations of SO2 from the satellite Suomi NPP OMPS: widespread air pollution events over China. Geophys. Res. Lett. 40, 4957–4962.
Yang, B., et al., 2017. Estimation of leaf area index and its sunlit portion from DSCOVR EPIC data: theoretical basis. Remote Sens. Environ. 198, 69–84.
Yang, E.G., et al., 2023. Using space-based CO2 and NO2 observations to estimate urban CO2 emissions. J. Geophys. Res. Atmos. 128, e2022JD037736.
Yin, Y., et al., 2020. Cropland carbon uptake delayed and reduced by 2019 Midwest floods. AGU Advances 1, e2019AV000140.
Yu, D., et al., 2021. Gravity recovery from SWOT altimetry using geoid height and geoid gradient. Rem. Sens. Environ. 265.
Zeiger, et al., 2022. Analysis of CYGNSS coherent reflectivity over land for the characterization of pan-tropical inundation dynamics. Rem. Sens. Environ. 282.
Zhang, A., et al., 2019. Evaluation of latest GPM-Era high-resolution satellite precipitation products during the May 2017 Guangdong extreme rainfall event. Atmos. Res. 216, 76–85.
Zhang, M., et al., 2023a. Solar-induced fluorescence helps constrain global patterns in net biosphere exchange, as estimated using atmospheric CO2 observations. J. Geophys. Res. Biogeosciences 128, e2023JG007703.
Zhang, Y., et al., 2023b. Satellite solar-induced chlorophyll fluorescence tracks physiological drought stress development during 2020 southwest US drought. Glob. Change Biol. 29, 3395–3408.
Zhang, Z., et al., 2023c. Large diurnal compensatory effects mitigate the response of Amazonian forests to atmospheric warming and drying. Sci. Adv. 9, eabq4974.
Zoogman, P., et al., 2014. Monitoring high-ozone events in the US Intermountain West using TEMPO geostationary satellite observations. Atmos. Chem. Phys. 14, 6261–6271.
Zoogman, P., et al., 2017. Tropospheric emissions: monitoring of pollution (TEMPO). J. Quant. Spectrosc. Radiat. Transf. 186.